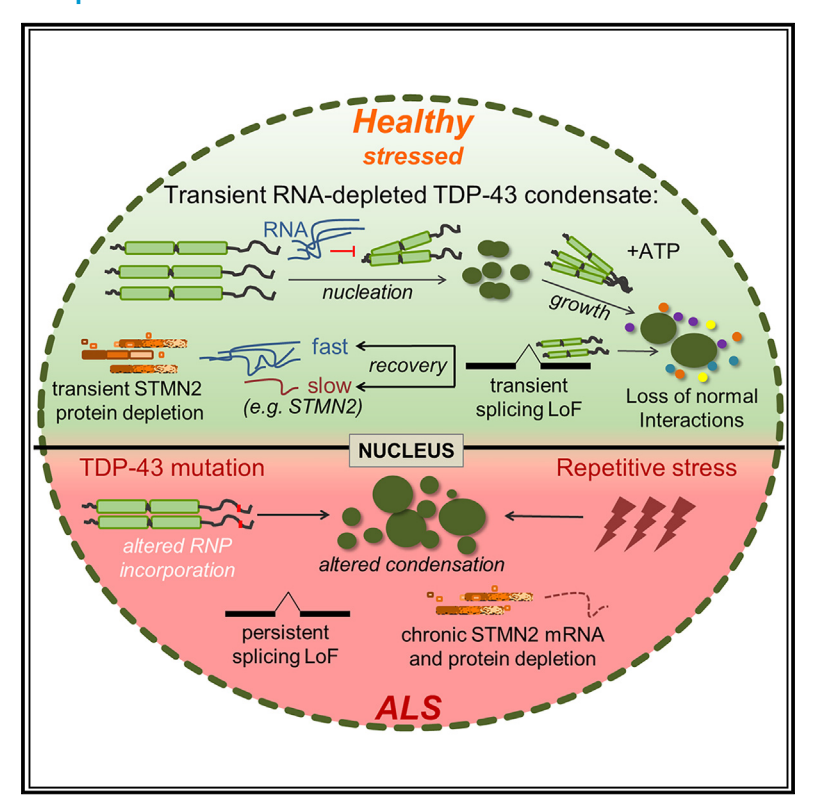
# Stress-induced TDP-43 nuclear condensation causes splicing loss of function and STMN2 depletion

#### **Graphical abstract**



#### **Authors**

Wan-Ping Huang, Brittany C.S. Ellis, Rachel E. Hodgson, ..., Jessica Rayment, Tobias Moll, Tatyana A. Shelkovnikova

#### Correspondence

t.shelkovnikova@sheffield.ac.uk

#### In brief

Cellular stress may contribute to neurodegeneration. Huang et al. demonstrate that stress-induced nuclear condensation of the neurodegeneration-linked TDP-43 protein causes its transient inactivation and loss of function in splicing. Although these changes are reversible, some TDP-43 splicing targets, e.g., STMN2, recover slowly, rendering them prone to misregulation under chronic stress.

#### **Highlights**

- Cellular stress induces RNA-depleted, non-liquid TDP-43 condensates in the nucleus
- ALS mutations affect nuclear TDP-43 condensation under stress
- Stress-induced nuclear condensation inactivates TDP-43, leading to splicing loss of function
- STMN2 splicing displays slow recovery post stress







#### **Article**

# Stress-induced TDP-43 nuclear condensation causes splicing loss of function and STMN2 depletion

Wan-Ping Huang, <sup>1,2</sup> Brittany C.S. Ellis, <sup>1,2</sup> Rachel E. Hodgson, <sup>1</sup> Anna Sanchez Avila, <sup>1</sup> Vedanth Kumar, <sup>1</sup> Jessica Rayment, <sup>1</sup> Tobias Moll, <sup>1</sup> and Tatyana A. Shelkovnikova <sup>1,3,\*</sup>

<sup>1</sup>Sheffield Institute for Translational Neuroscience and Neuroscience Institute, University of Sheffield, Sheffield, UK

#### **SUMMARY**

TDP-43 protein is dysregulated in several neurodegenerative diseases, which often have a multifactorial nature and may have extrinsic stressors as a "second hit." TDP-43 undergoes reversible nuclear condensation in stressed cells including neurons. Here, we demonstrate that stress-inducible nuclear TDP-43 condensates are RNA-depleted, non-liquid assemblies distinct from the known nuclear bodies. Their formation requires TDP-43 oligomerization and ATP and is inhibited by RNA. Using a confocal nanoscanning assay, we find that amyotrophic lateral sclerosis (ALS)-linked mutations alter stress-induced TDP-43 condensation by changing its affinity to liquid-like ribonucleoprotein assemblies. Stress-induced nuclear condensation transiently inactivates TDP-43, leading to loss of interaction with its protein binding partners and loss of function in splicing. Splicing changes are especially prominent and persisting for STMN2 RNA, and STMN2 protein becomes rapidly depleted early during stress. Our results point to early pathological changes to TDP-43 in the nucleus and support therapeutic modulation of stress response in ALS.

#### INTRODUCTION

TDP-43 is one of the most studied proteins linked to neurodegenerative diseases of aging, such as amyotrophic lateral sclerosis (ALS), frontotemporal dementia (FTD), and Alzheimer's disease. Wild-type (WT) TDP-43 presents with abnormal distribution patterns in the central nervous system in these conditions, including nuclear clearance and excessive cytoplasmic accumulation, sometimes accompanied by the formation of aggregates/inclusions. In addition, >50 ALS/FTD-linked variants have been reported in the encoding gene, TARDBP. TDP-43 is an abundant RNA/DNA-binding protein (RBP) splicing factor. Unsurprisingly, splicing deficiencies downstream of TDP-43 dysfunction in neurons cause a spectrum of cellular pathologies, with axonal defects due to STMN2 depletion being the most characterized. 8–10

TDP-43 can oligomerize and is capable of phase transitions, including liquid-liquid phase separation (LLPS); it enters and/or interacts with several biomolecular condensates, or membraneless organelles (MLOs), in the nucleus and cytoplasm. TDP-43 self-association is required for its MLO partitioning. Cellular stress triggers a whole array of changes in the condensate/MLO metabolism, augmenting the assembly of some condensates while dispersing others, as well as inducing *de novo* MLO formation. TDP-43 responds to stress by changing its localization, e.g., undergoing a partial shift to the cytoplasm

or recruitment into MLOs/condensates such as stress granules, nuclear stress bodies, or promyelocytic leukemia (PML) bodies. <sup>15–17</sup> Neurodegenerative diseases have a multistep pathogenesis, whereby different factors, including cellular stresses, may contribute to the molecular pathology development. <sup>18</sup> Today we have a fairly good knowledge of the endstage TDP-43 pathologies from postmortem tissue studies, including proteinaceous inclusion formation. However, very little is still known about the early changes to TDP-43 in the nucleus, including under stress, which may lead to these disease hallmarks.

Here we demonstrate, using chemically induced changes as a stress paradigm, that TDP-43 transiently forms RNA-depleted assemblies with low dynamic properties in the nucleus of stressed cells including human neurons. We further establish that ALS-linked mutations alter either nucleation of these condensates or their dynamic properties. These condensates inactivate TDP-43, leading to loss of function in splicing, and although these changes are reversible, splicing recovery rates differ for different transcripts, with STMN2 RNA displaying slow recovery. Our study describes a stress-responsive regulatory mechanism for TDP-43 function in splicing executed via its reversible sequestration into an RNA-depleted MLO in the nucleus. These findings shed light on the stress-related changes to the nuclear TDP-43 metabolism that can contribute to the pathogenesis of ALS and related diseases.



<sup>&</sup>lt;sup>2</sup>These authors contributed equally

<sup>&</sup>lt;sup>3</sup>Lead contact

<sup>\*</sup>Correspondence: t.shelkovnikova@sheffield.ac.uk https://doi.org/10.1016/j.celrep.2024.114421



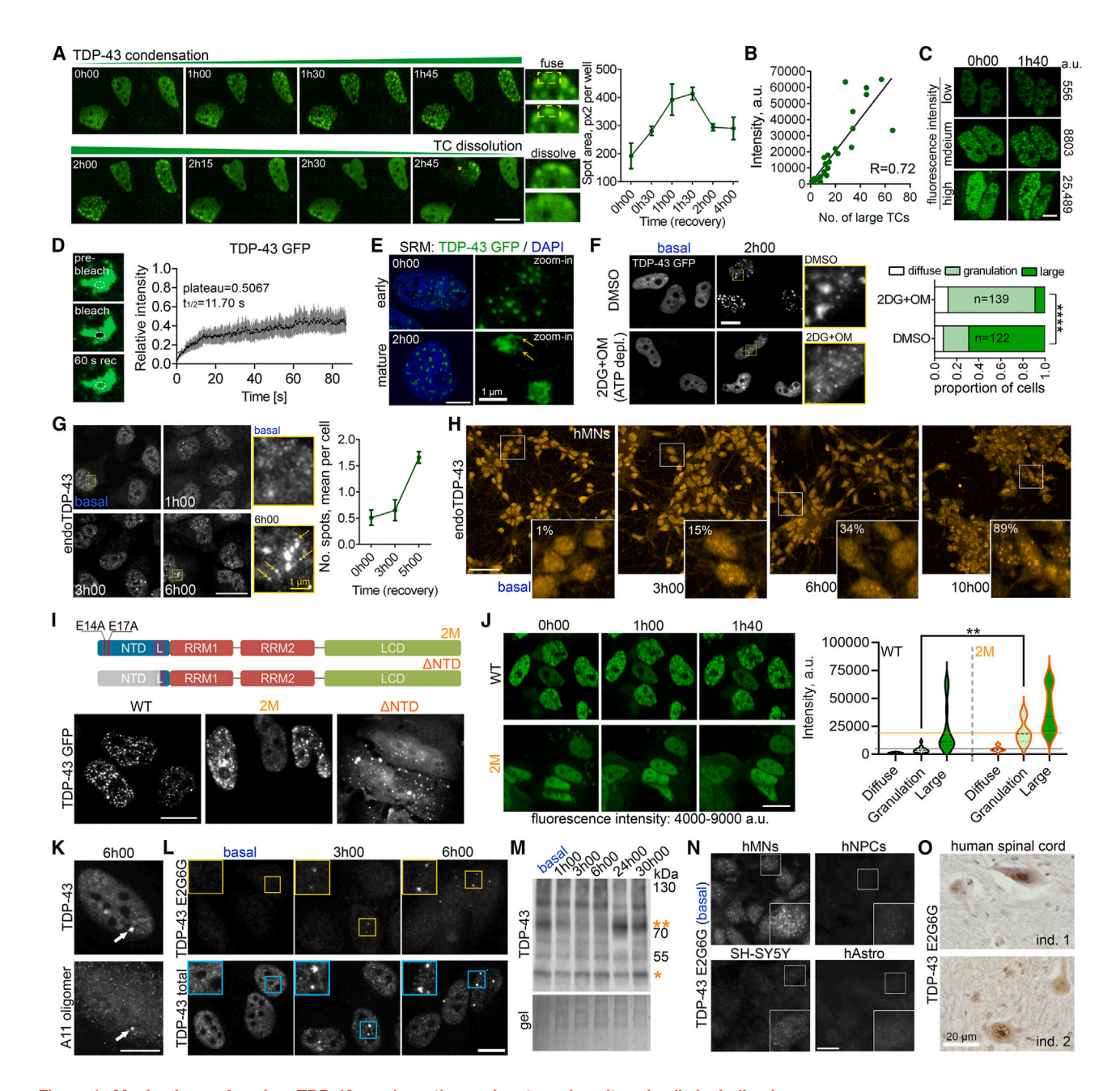


Figure 1. Mechanisms of nuclear TDP-43 condensation under stress in cultured cells including human neurons

(A) Dynamics of nuclear TDP-43 condensation in response to arsenite (NaAsO $_2$ ) stress. TDP-43 condensates (TCs) formed by ectopically expressed GFP-tagged TDP-43 were tracked by high-content confocal imaging (>150 cells per time point from three wells). Asterisk indicates a dying cell. Scale bar, 10  $\mu$ m.

(B and C) TDP-43 condensation is concentration dependent and has a low nucleation threshold. TC assembly correlates with TDP-43 GFP fluorescence intensity at the baseline (B). Fluorescence intensity was measured in individual cells immediately after NaAsO<sub>2</sub> wash-off (0h00) and after 2 h of recovery. 524 TCs from 27 cells were analyzed. In (C), representative images for cells with the lowest ( $10^{th}$  percentile), highest ( $99^{th}$  percentile), and intermediate expression and the corresponding GFP fluorescence intensity are shown for the 2-h recovery time point. a.u., arbitrary units. Scale bar, 5  $\mu$ m.

- (D) Incomplete fluorescence recovery (early plateau) for TCs as measured by FRAP. TDP-43 GFP-expressing cells were analyzed 2 h into recovery from NaAsO<sub>2</sub> stress. Experiment was repeated three times, with ten cells and three condensates in each nucleus analyzed in every repeat.
- (E) Super-resolution microscopy (SRM) detects diffraction-limited TC "cores" and the substructure of the large ( $\geq 1~\mu m$ ) assemblies (mature TCs) formed by ectopically expressed TDP-43. Arrows indicate individual cores within mature TCs. Scale bar, 5  $\mu m$ .
- (F) TCs require ATP for their growth/higher-order assembly. Cells were pre-treated with oligomycin A (OM) and 2-deoxyglucose (2-DG) for 1 h prior to NaAsO<sub>2</sub> stress. Number of cells analyzed (20 fields of view) is indicated within bars; \*\*\*\*p < 0.0001 (large/mature TCs), one-way ANOVA with Holm-Sidak test. Scale bar, 10  $\mu$ m.

(legend continued on next page)

#### **Article**



#### **RESULTS**

### Determinants of stress-induced TDP-43 condensation in the nucleus

Previous studies have reported visible TDP-43 granulation in the nucleus during recovery from arsenite (NaAsO<sub>2</sub>) stress. 19-21 To better understand this process, we first employed time-lapse confocal imaging of TDP-43 GFP-expressing HeLa cells. This analysis demonstrated a dynamic behavior of these de novo TDP-43 nuclear condensates (TCs hereafter), with individual structures growing in size (maximum assembly at ~1 h 45 min of recovery) and subsequently fully dissolving (Figure 1A). Ectopically expressed TDP-43 did not form condensates spontaneously, without stress exposure, even in high-expressing cells (Figure S1A). TC assembly was concentration dependent, where higher fluorescence intensity at the baseline positively correlated with formation of large (>1  $\mu$ m) TCs (r = 0.72) (Figure 1B). However, "fine" granulation was readily detectable in cells with very low TDP-43 expression (below the 10<sup>th</sup> percentile), indicating a low assembly threshold (Figure 1C). Although mature/end-stage TCs demonstrated fluorescence recovery after photobleaching (Figure 1D), it was relatively slow ( $t_{1/2} = 9.28-15.04$  s, mean = 11.70 s), and full recovery was not achieved (plateau between 0.4887 and 0.5260, mean = 0.5067), suggesting restricted mobility of TDP-43 within the structures. Super-resolution microscopy (SRM) revealed that the smallest, diffraction-limited TCs (TC "cores") represent uniformly sized (~100 nm) granules, whereas the larger structures correspond to their higher-order assemblies (Figure 1E), although remodeling during coalescence cannot be ruled out.

We next asked whether stress-induced TDP-43 condensation is an active process. TDP-43 GFP-expressing cells were pretreated with a combination of 2-deoxyglucose (2DG) and oligomycin A (OM) to block glycolysis and oxidative phosphorylation, respectively, leading to rapid ATP depletion, <sup>22</sup> and analyzed during the recovery from NaAsO<sub>2</sub>. Although TC nucleation was not affected by ATP depletion (the majority of cells still showing granulation), it prevented TC growth, with very few 2DG/OM-treated cells forming large TCs (Figure 1F).

Endogenous TDP-43 also readily formed TDP-43-positive granules ("endoTCs") in HeLa and SH-SY5Y cells, with a slower assembly kinetic, peaking at 5–6 h into the recovery (Figures 1G and S1B) and fully resolving 16 h into the recovery (Figures 1C). EndoTC cores were similar in size to the cores formed by TDP-43 GFP (~100 nm) (Figures 1G and S1D). TDP-43 condensation could also be induced by proteasomal inhibition, viral mimic poly(I:C), or heat stress (Figures S1E and S1F). We also confirmed the ATP requirement for endoTC growth (Figure S1G). Finally, we found that motor neurons derived from human embryonic stem cells (hMNs) $^{23}$  also form TCs during the recovery from NaAsO<sub>2</sub>, although their assembly was delayed compared to non-neuronal cells (peak assembly at ~10 h of recovery) (Figure 1H).

The C-terminal domain (CTD) of TDP-43 was previously found to be required for its nuclear condensation. 19 Since the N-terminal domain (NTD) also contributes to TDP-43 self-association, 12,24 we examined TC-forming behavior of a mutant lacking NTD ( $\Delta$ NTD) and a "mild" NTD mutant (two point mutations E14A/E17A: "2M") (Figures 1I and S1H). While the 2M mutant was still able to form TCs, the ΔNTD mutant lost this ability, even in cells with high expression (Figure 1I). Tracking TDP-43 condensation in individual cells by time-lapse imaging revealed that the 2M mutant requires significantly higher levels for TC nucleation than WT, on average 4.9-fold higher (as measured by fluorescence intensity, mean 19,859 vs. 4051 a.u. for 2M and WT TDP-43, respectively) (Figure 1J). Overall, only 48.7% of 2M-expressing cells had visible granulation after 2 h of recovery, compared to 91.8% of WT cells. Therefore, intact TDP-43 NTD is essential for TC nucleation whereas ATP is required for their arowth.

TDP-43 was previously shown to localize to nuclear stress bodies (nSBs) under heat-stress conditions, <sup>16</sup> and nSBs can be induced by NaAsO<sub>2</sub>. <sup>25</sup> We found no overlap between nSBs and endoTCs induced by either heat shock or NaAsO<sub>2</sub> (Figures S2A and S2B). TDP-43 is enriched in several constitutive nuclear bodies. <sup>17,24,26</sup> TCs, however, showed no overlap with splicing speckles, Cajal bodies, or PML bodies (Figures S2B and S2C). Interestingly, the latter three nuclear bodies appeared to physically interact with TCs (Figures S2B and S2C), likely due to TDP-43 transfer from these structures into TCs. TDP-43 is a

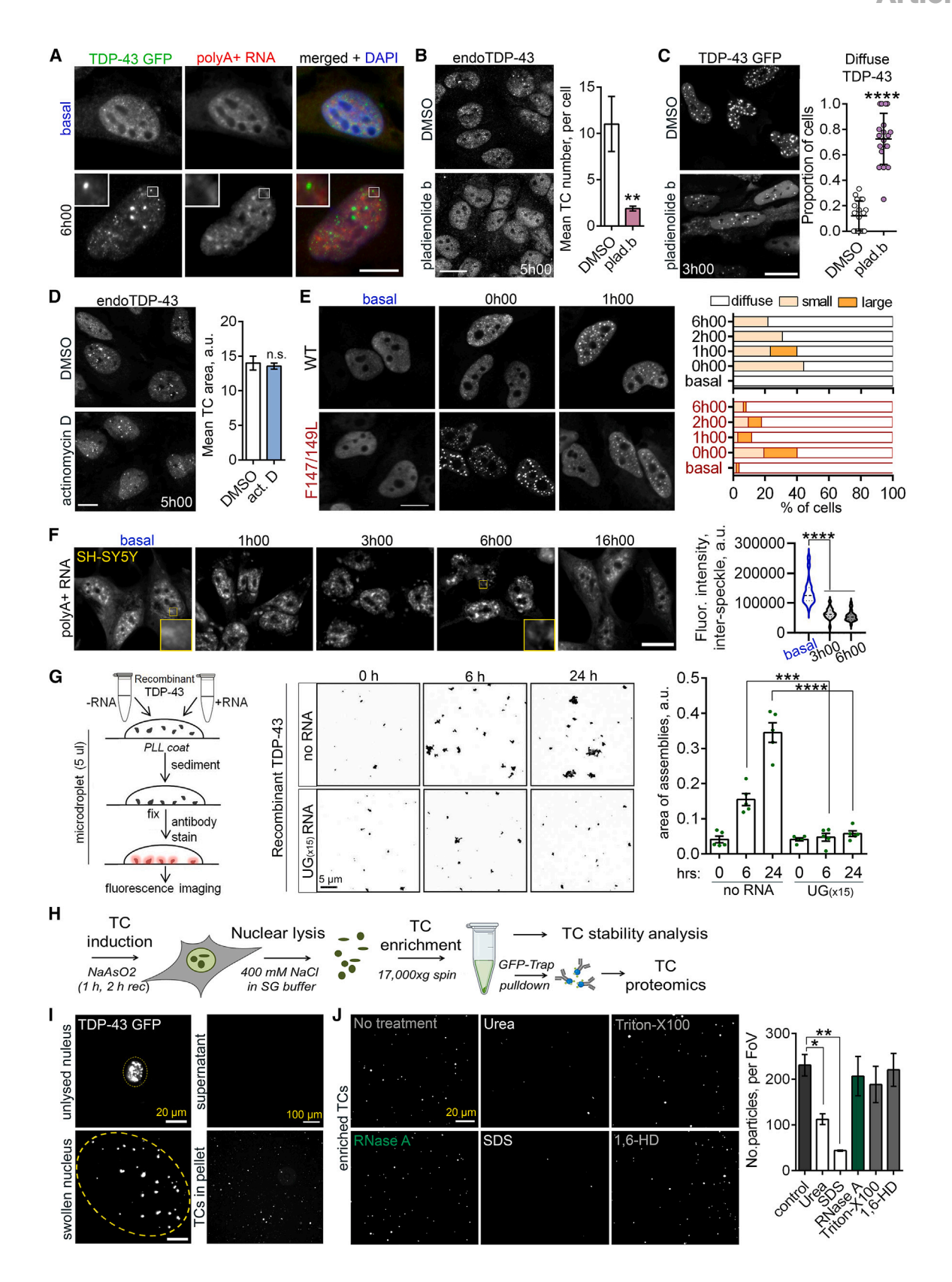
(G) Endogenous TDP-43 forms TCs (endoTCs) with the core size similar to the ectopically expressed protein but with a slower kinetic. Arrows indicate TC cores. More than 400 cells from three wells were analyzed per time point using automated imaging/quantification. Scale bar, 20 μm.

(H) Human embryonic stem cell (hESC)-derived motor neurons (hMNs) form TCs during the recovery from NaAsO<sub>2</sub> with a slow assembly kinetic. Day-42 hMNs were used. Percentage of cells positive for TCs at each time point (three fields of view) is indicated. Scale bar, 20  $\mu$ m.

(I and J) Nuclear TDP-43 condensation requires its N-terminal domain (NTD). "Mild" TDP-43 NTD mutant (2M), but not the variant with NTD deleted, retains condensation ability (I), but has a higher granulation threshold as compared to WT (J). Cells were analyzed at 2 h into recovery as the endpoint assembly (I, and graph in J). Mean thresholds for onset of granulation are indicated with black and orange lines for WT and 2M, respectively. N = 49 and 39 cells (from three wells) for WT and 2M, respectively. \*\*p < 0.01, unpaired t test. Scale bar, 10  $\mu$ m.

- (K) EndoTCs are positive for A11-oligomer antibody that recognizes β-sheet structure. Scale bar, 5 μm.
- (L) EndoTCs are enriched in non-NTD oligomerized TDP-43. Scale bar, 10  $\mu m.\,$
- (M) Stress induces a reversible decline in TDP-43 dimer. SH-SY5Y cells were analyzed during the recovery from NaAsO<sub>2</sub> stress by western blotting of DSG-crosslinked samples with a C-terminal TDP-43 antibody. Double and single asterisks indicate TDP-43 dimer and monomer, respectively.
- (N) High basal levels of non-NTD-oligomerized TDP-43 in hMNs. NPCs, astrocytes, and hMNs were differentiated from the same hESC line. SH-SY5Y cells were also included as a neuron-like cell line. Note that insets represent overexposed images. Scale bar, 10 µm.
- (O) High levels of non-NTD-oligomerized TDP-43 in the nucleus of human spinal neurons. Representative images for the spinal cord for two individuals are shown. HeLa cells were used unless indicated otherwise. In all panels, time points indicate the recovery from  $NaAsO_2$  stress. In all cases, quantification data and/or images are from a representative experiment repeated three times (N = 3); number of technical replicates (fields of view, wells, or individual cells for FRAP) is indicated for each panel.





(legend on next page)



paraspeckle component,<sup>27,28</sup> and NEAT1 long non-coding RNA, the most reliable paraspeckle marker, was found to be enriched in TCs.<sup>19</sup> Our detailed analysis of the relationship between TCs and paraspeckles revealed a clear distinction between the two structures.<sup>29</sup> Thus, TC is a condensate distinct from the known nuclear bodies.

Given the low mobility of TDP-43 within TCs according to fluorescence recovery after photobleaching (FRAP), we asked whether these structures are amyloid-like, similar to TDP-43 myogranules.  $^{30}$  Indeed, TCs formed by ectopically expressed and endogenous TDP-43 were reactive with the A11-oligomer antibody (Figures 1K and S1I) that recognizes  $\beta$ -sheet-rich structures.  $^{31}$ 

Recently, it has been reported that TDP-43 not oligomerized via its NTD can be detected with an antibody recognizing an epitope on the dimer surface.<sup>32</sup> Using this monoclonal antibody (E2G6G), we studied the levels and distribution of non-NTD-oligomerized TDP-43, by immunostaining, during the recovery from NaAsO<sub>2</sub>. TDP-43 E2G6G positive species were almost undetectable in HeLa cells under basal conditions but accumulated during the recovery from stress (Figure 1L). Using disuccinimidyl glutarate (DSG) crosslinking, 12,33 a corresponding decline in TDP-43 dimer was observed (Figure 1M). Strikingly, we found that E2G6G antibody readily detects endoTCs and TCs formed by TDP-43 GFP (Figures 1L and S1J). Previously it was reported that in vitro, TDP-43 can initially oligomerize via its NTD, bringing the CTDs in proximity and allowing subsequent higher-order assembly to proceed via CTD-CTD interactions.<sup>34</sup> TC positivity for E2G6G antibody is in line with this model and with the TDP-43 CTD requirement for its condensation.<sup>19</sup>

We next asked whether the relatively slow TC assembly in hMNs (detectable from 6 h of recovery, Figure 1H) is due to the difference in the basal level of non-NTD-oligomerized TDP-43. Indeed, we observed high TDP-43 E2G6G immunoreactivity in the nucleus of hMNs, in contrast to day-16 neural precursors (NPCs), astrocytes differentiated from the same stem cell line, or SH-SY5Y cells (Figure 1N), whereas the reactivity for "total" TDP-43 was similar across these cell types (Figure S1K). This

prompted us to perform TDP-43 E2G6G analysis in the human spinal cord. In line with the cellular data, spinal neurons, but not glial cells, displayed a significant TDP-43 E2G6G immunore-activity in the nucleus (Figure 10). Thus, high steady-state level of non-NTD-oligomerized TDP-43, and hence lower levels of pre-existing NTD-NTD interactions, may contribute to the delayed TC nucleation in hMNs.

To conclude, in stress conditions, TDP-43 forms nuclear condensates with an internal substructure and low dynamic properties that are distinct from known nuclear bodies. This is an active, ATP-dependent process that is initiated by TDP-43 NTD-driven self-association. High basal levels of non-NTD-oligomerized TDP-43 in hMNs may delay the onset of its condensation during stress.

### Stress-induced nuclear TDP-43 condensates are negatively regulated by RNA

Although the majority of nuclear condensates are RNA-rich granules,<sup>35</sup> using oligo(dT) RNA-fluorescence in situ hybridization (FISH), we unexpectedly found that TCs formed by endogenous or ectopically expressed TDP-43 are depleted of polyadenylated RNA (Figures 2A and S3A). Because TDP-43 preferentially binds to intronic UG-rich sequences, 36 we analyzed TC assembly in cells pre-treated with a splicing inhibitor (pladienolide B) to induce pre-mRNA accumulation. This pre-treatment led to diminished TC assembly by endogenous and ectopically expressed TDP-43 during the recovery from NaAsO<sub>2</sub> (Figures 2B and 2C). GFP-expressing cells in TDP-43 pre-treated with pladienolide B also had a dramatically reduced number of small TDP-43 foci (14  $\pm$  6 per cell vs. 143  $\pm$  52 in DMSO-treated cultures), with the protein remaining largely diffuse during the recovery from NaAsO $_2$  (Figure 2C), suggesting that RNA inhibits the TC nucleation step. Pre-treatment with actinomycin D for 3 h (which causes only minor TDP-43 redistribution to the cytoplasm in this cell line<sup>37</sup>) did not prevent TC assembly (Figure 2D). Finally, a TDP-43 mutant with disrupted RNA binding, F147/149L,<sup>38</sup> displayed accelerated TC assembly with an increased proportion of large TCs early after NaAsO2 removal (Figure 2E). These

#### Figure 2. Stress-induced nuclear TDP-43 condensation is inhibited by (UG-rich) RNA

(A) Polyadenylated RNA is depleted from endoTCs. HeLa cells were used. Scale bar, 10  $\mu m$ .

(B and C) Pre-mRNA accumulation induced by splicing inhibition limits TC assembly. Cells were pre-treated with pladienolide B for 1 h prior to NaAsO<sub>2</sub> stress. In (B), 77 and 128 cells (five and seven fields of view) were analyzed for DMSO and pladienolide B conditions, respectively; \*\*p < 0.01, unpaired t test. In (C), 95 and 94 TDP-43 GFP-expressing cells (20 fields of view) were analyzed for DMSO and pladienolide B conditions, respectively; \*\*\*\*p < 0.0001, unpaired t test. Error bars represent SD. Scale bars, 15  $\mu$ m.

(D) RNA depletion prior to stress does not prevent nuclear condensation of endogenous TDP-43. Cells were pre-treated with actinomycin D for 1 h prior to NaAsO<sub>2</sub> stress. More than 500 cells from three wells were analyzed per condition using automated imaging.

(E) Disrupted RNA binding promotes stress-induced nuclear TDP-43 condensation. TDP-43 F147/149L mutant (FLAG-tagged) forms TCs earlier/more efficiently than WT TDP-43.  $\geq$ 100 cells ( $\geq$ 10 fields of view) were quantified per condition/time point, manually, in a blinded manner. Scale bars, 10  $\mu$ m.

(F) Polyadenylated RNA undergoes segregation in the nucleoplasm during the recovery from NaAsO<sub>2</sub> stress leading to its depletion from interspeckle space. SH-SY5Y cells were used in this experiment due to prominent speckle localization of polyA<sup>+</sup> RNA. 36, 38, and 27 nuclei, three regions of interest (ROIs) in each, were analyzed for basal, 3 h, and 6 h recovery time points, respectively. \*\*\*\*\*p < 0.0001, Kruskal-Wallis test with Dunn's post hoc test.

(G) Analysis of in vitro TC-like TDP-43 assemblies. Time-dependent changes in the size of recombinant TDP-43 assemblies and their abundance in the presence or absence of  $(UG)_{x15}$  RNA oligonucleotide are shown. Data points are fields of view; \*\*\*p < 0.001, \*\*\*\*p < 0.0001, one-way ANOVA with Holm-Sidak test.

(H) Experimental pipeline for TC purification from cells. SG buffer, buffer used for the isolation of stress granule cores (see STAR Methods for details). (I and J) Purified TCs are insensitive to RNase A, 1,6-hexanediol, and Triton X-100. In (I), examples of TC-containing nuclei prior to lysis, swollen semi-lysed nuclei, and TCs isolated by centrifugation are shown (see also Video S1). In (J), TCs enriched by centrifugation were treated as indicated for 30 min, and TC number was quantified at  $\times$ 20 magnification in five fields of view (FoV). \*p < 0.05, \*\*p < 0.01, Kruskal-Wallis test with Dunn's post hoc test.

In all cases, quantitative data and/or images are from a representative experiment repeated three times (N = 3); number of technical replicates (fields of view, wells, or individual nuclei/cells) is indicated for each panel.



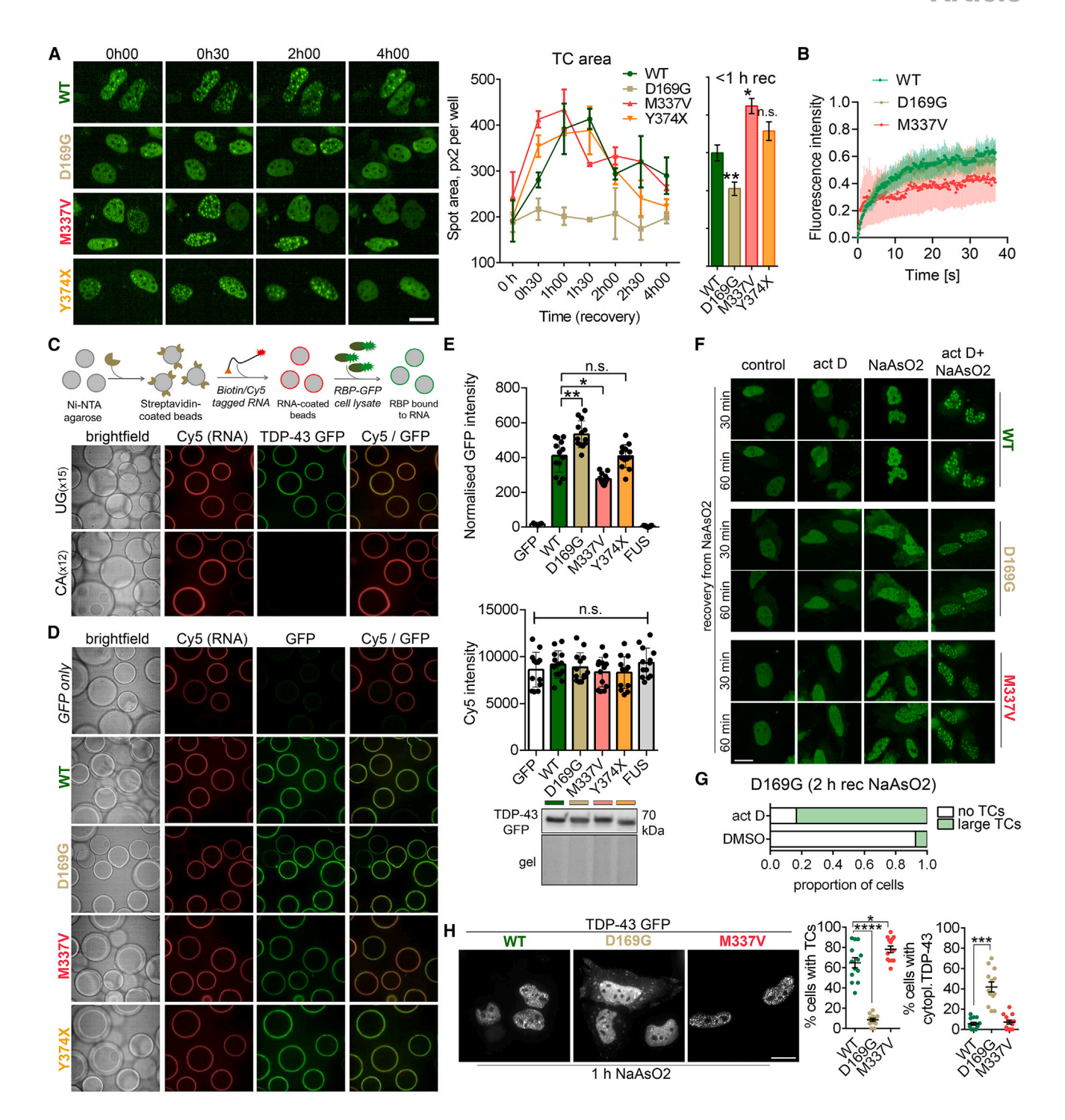


Figure 3. ALS mutations impact stress-induced nuclear TDP-43 condensation by affecting RNP binding

(A) Differential effect of ALS mutations on TDP-43's condensation propensity in the nucleus during the recovery from NaAsO<sub>2</sub>. Representative images and automated quantification from high-content confocal imaging are shown. More than 150 cells were analyzed per condition/time point (2 wells); right graph shows combined data for the two early time points.  $^*p < 0.05$ ,  $^*p < 0.01$ , one-way ANOVA with Holm-Sidak post hoc test. Scale bar, 10  $\mu$ m.

(B) FRAP analysis reveals deficiencies in TDP-43 mobility within TCs for M337V but not D169G variant. Cells were analyzed 2 h into the recovery from NaAsO<sub>2</sub>. Ten cells (three condensates in each) were analyzed for each TDP-43 variant.

(C–E) CONA (confocal nanoscanning) assay reveals altered mutant TDP-43 affinity to UG-RNA-nucleated RNP complexes. Assay schematic and the effect of RNA sequence (C), representative images (D), and quantification (E) of ring intensities for TDP-43 GFP and Cy5 (RNA) are shown. Western blot was used to

(legend continued on next page)

#### **Article**



phenotypes were fully recapitulated when a proteasomal inhibitor, MG132, was used to induce TCs (Figures S3B-S3D).

Having shown that (UG-rich) RNA limits stress-induced TDP-43 condensation in the nucleus, we investigated possible changes to the nucleoplasmic RNA distribution during stress. This analysis was performed in SH-SY5Y cells that have prominent polyA+ RNA-positive speckles. In addition to speckles, polyA+ RNA was detected in cytoplasmic stress granules at the early recovery time points, consistent with a previous report.<sup>39</sup> Although the polyA<sup>+</sup> RNA signal remained high in the nucleus throughout the recovery from NaAsO2, it underwent spatial segregation, with the signal density increasing in speckles from 3 h of recovery onward (Figure 2F). As a result, the interspeckle space, where TCs form (Figures S2B and S2C, pinin [PNN] marker), became depleted of RNA (Figure 2F). Therefore, stress-induced nucleoplasmic remodeling associated with spatial RNA segregation may create favorable conditions for TC nucleation.

We next sought to use an in vitro approach to validate the effect of RNA on TDP-43 assemblies. Using an immunodetection protocol we have recently developed,<sup>29</sup> we found that untagged recombinant TDP-43 spontaneously forms large (>1 μm) assemblies, and their number and size increase with time in a physiological salt buffer (Figures 2G and S4A). These assemblies were reminiscent of cellular TCs in their morphology and timedependent growth and hence were used as an in vitro TC mimic. TDP-43 assemblies were analyzed at 0, 6, and 24 h post thawing in the presence or absence of synthetic UG<sub>(x15)</sub> RNA oligonucleotide, which allows efficient multivalent binding. 40 In line with the cellular data, RNA addition almost prevented time-dependent growth of in vitro TDP-43 assemblies (Figure 2G), and total RNA from HeLa cells had a similar effect (data not shown). We also analyzed the effect of RNA on the smaller clusters of recombinant TDP-43 that mimic TC "cores." Consistently, (UG)x15 RNA, but not a non-target sequence  $(CA)_{x12}$ , dissolved these clusters after a 24-h incubation (Figure S4B).

To directly interrogate the role of RNA in the maintenance of TCs, we prepared a TC-enriched fraction from stressed HeLa cells expressing TDP-43 GFP (Figures 2H and 2I; Video S1) by adapting a protocol developed for paraspeckle isolation. TCs released from the nuclei were found to be stable assemblies that remained intact in the lysis buffer for several hours. Using a panel of agents known to affect the stability of biomolecular condensates, we found that TCs are dissolved by urea or SDS but withstand 1,6-hexanediol or Triton X-100 exposure (Figures 2I and 2J), consistent with the data for recombinant TDP-43 assemblies (Figure S4A). In agreement with the cellular data, purified TCs were insensitive to RNase A (Figures 2I and 2J).

Thus, stress-induced nuclear TDP-43 condensates are RNA-depleted assemblies whose nucleation is inhibited by (UG-rich) RNA. *Ex cellulo* studies also confirmed the non-LLPS nature of these assemblies.

### TDP-43 ALS mutants display defects in stress-induced nuclear condensation

To analyze the effect of ALS-linked TDP-43 mutations on its partitioning into TCs, we selected three ALS TDP-43 mutations affecting different domains of the protein: D169G (RRM1), M337V (low-complexity domain [LCD]), and a recently reported truncating mutant, Y374X (LCD). 42 The D169G mutant was previously found to compromise TDP-43 nuclear condensation, 19 but the mechanism remained unclear. Time-lapse imaging demonstrated that TDP-43 condensation during the recovery from NaAsO<sub>2</sub> is enhanced by M337V, attenuated by D169G, and not affected by Y374X mutation (Figures 3A and 3B). Similar results were obtained for proteasomal inhibition (Figure S5). By FRAP, TDP-43 M337V was less mobile in TCs, whereas in those D169G-expressing cells that did form TCs, the intra-TC mobility of this variant was similar to that of WT (mean  $t_{1/2} = 5.51$ , 4.73, and 10.75 s for WT, D169G, and M337V, respectively; Figure 3B). This indicated that D169G affects TC nucleation whereas M337V affects their dynamic properties.

Both D169G and M337V do not significantly affect RNA binding<sup>40,43</sup>; however, TDP-43 mutations were previously shown to affect the liquid properties of RNA-TDP-43 assemblies even in the absence of RNA-binding defects. 40,44 To test whether these mutations modulate TDP-43's affinity to LLPS ribonucleoprotein (RNP) complexes, we developed a quantitative microbead assay using the CONA (on-bead confocal nanoscanning) technique. 45 This approach employs confocal imaging of the cross-sections of functionalized beads, producing a fluorescent "ring" image whose intensity corresponds to the amount of the bound molecule (Figure 3C). The use of whole-cell lysates in this assay allows preservation of the complex cellular environment and natural protein interactions (i.e., semicellular conditions). A streptavidin "bridge" was used to functionalize nickel microbeads with biotinylated and fluorescently labeled synthetic RNA oligonucleotides. Incubation of beads coated with UG(x15)-Cy5 RNA with the lysate of TDP-43 GFP-expressing cells yielded a bright GFP ring, whereas no ring was observed when beads were coated with CA<sub>(x12)</sub>-Cy5 RNA (Figures 3C and S6A-S6C). No ring was visible for GFP alone or the RNA-binding-deficient TDP-43 F147/149L variant (Figures 3D and S6D). We used the fluorescence intensity of the GFP ring as readout for TDP-43 ability to enter RNA-nucleated RNP assemblies. An automated pipeline for CONA quantification that allows rapid analysis of

confirm equal protein loading to beads (E). In (D) and (E), (UG)<sub>x15</sub> RNA was used. At least ten fields of view were analyzed per condition; \*p < 0.05, \*\*p < 0.01, one-way ANOVA with Dunnett's post hoc test (n.s., not significant). See Figure S6 for details of assay development.

<sup>(</sup>F and G) RNA depletion rescues the condensation defect of TDP-43 D169G mutant. Cells pre-treated with actinomycin D for 2 h prior to NaAsO<sub>2</sub> stress. Representative images for all variants (F) and quantification for D169G mutant (G) are shown. Twenty-seven and 30 cells (ten fields of view) were analyzed for DMSO and actinomycin D, respectively. Scale bar. 10 µm.

<sup>(</sup>H) Deficient nuclear TDP-43 condensation correlates with its cytoplasmic redistribution early during stress. More than 100 cells (13 fields of view) were analyzed per condition. \*p < 0.05, \*\*p < 0.01, \*\*\*\*p < 0.001, one-way ANOVA with Dunnett's post hoc test. Scale bar, 10  $\mu$ m.

In all cases, quantification data and/or images are from a representative experiment repeated three times (N = 3); number of technical replicates (fields of view, wells, or individual cells for FRAP) is indicated for each panel.



hundreds of beads was developed (Figure S6E). CONA analysis revealed that D169G significantly increases, M337V significantly decreases, and Y374X has no effect on TDP-43 GFP ring fluorescence intensity as compared to WT protein (Figures 3D and 3E). Thus, M337V reduces while D169G augments TDP-43's ability to incorporate into LLPS RNP complexes, which inversely correlates with their competency in TC assembly. To further confirm that the high affinity of the D169G mutant to RNPs prevents efficient TC nucleation, we performed RNA depletion to disrupt such complexes, prior to NaAsO<sub>2</sub> stress. Indeed, actinomycin D pre-treatment was sufficient to rescue TC nucleation deficiency of the D169G variant (Figures 3F and 3G).

Recruitment into macromolecular complexes has been shown to retain TDP-43 in the nucleus.  $^{46,47}$  In line with this, we found that TC-deficient D169G, but not TC-forming M337V and Y374X variants, displayed significant redistribution to the cytoplasm early during recovery from NaAsO<sub>2</sub> (1 h) (Figure 3H and data not shown).

Therefore, TDP-43 ALS mutants display altered stress-induced condensation, which correlates with their impact on TDP-43's ability to enter RNA-nucleated complexes. Furthermore, nuclear TDP-43 condensation regulates its cytoplasmic levels during stress.

# Stress-induced nuclear TDP-43 condensation leads to reversible loss of its solubility and functional interactions

We next sought to characterize the functional consequences of stress-induced nuclear TDP-43 condensation. In our experiments with ectopic protein expression we noticed dramatic, nearly complete TDP-43 depletion from the nucleoplasm upon TC assembly (Figure 4A). Consistently, FRAP experiments with bleaching of the entire TC revealed slow and inefficient fluorescence recovery, consistent with low levels of "free" TDP-43 in the nucleoplasm (Figure 4B). Quantification of the diffuse nucleoplasmic pool of endogenous TDP-43 confirmed its nucleoplasmic depletion during the recovery from NaAsO<sub>2</sub> (Figure 4C). This analysis also revealed that cytoplasmic TDP-43 relocalization was an early and very transient event during stress, whereas TDP-43 nucleoplasmic depletion occurred later, correlated with TC assembly, was uncoupled from the cytoplasmic redistribution, and persisted for longer (Figure 4C). Endogenous TDP-43 condensation correlated well with a reduction in its solubility in fractionation experiments (shift from supernatant to pellet fraction, Figure 4D). In line with this, heating-step omission for "total protein" samples prepared by direct cell lysis in SDS-PAGE buffer led to strikingly low TDP-43 monomer detection in the "stressed" samples (Figure S7A), indicating its severely reduced solubility. Loss of TDP-43 solubility was evident prior to the assembly of visible TCs (as early as 1 h of recovery) (Figures 4D and S7A), raising the possibility that its "fine" condensation, not detectable by the regular fixation-immunostaining protocol, occurs at the earliest recovery stages. Indeed, removal of the soluble nucleoplasmic protein by formamide "extraction" revealed increased TDP-43 granulation in the nucleus at the 1-h recovery time point (Figure 4E).

We next performed affinity purification of TCs formed by TDP-43 GFP and enriched as described above (Figure 2H) using GFP-

Trap agarose, followed by mass spectrometry analysis of their composition (Figures S7B and S7C). In total, 168 proteins were identified as relatively enriched compared to GFP-only samples (Table S1). We next compared the TC proteome with two published TDP-43 interactomes. 48,49 Only eight proteins (4.8% of the TC dataset) were found in common between the three datasets (Figure 4F). Biological process gene ontology (GO) term analysis revealed that TCs are severely depleted of RNA metabolism factors—the primary TDP-43 interactors (Figure 4G and Table S1). On the other hand, some interactions were gained in TCs compared to the TDP-43 interactome, e.g., those related to stress response, ATP metabolism, and chromosome condensation (Figures 4G and 4H), consistent with TC's ATP dependence and dramatic nuclear remodeling during stress. However, the number of proteins in these categories was low (a maximum of 13 in the top GO terms compared to >70 in the soluble TDP-43 interactome) (Table S1). We also performed pull-down of soluble nuclear TDP-43 GFP in the same cell line, followed by mass spectrometry. Only 8.2% of TDP-43 GFP interactors identified in this analysis were also present in the TC proteome, confirming loss of multiple binding partners by TDP-43 upon TC sequestration (Figures S7D and S7E; Table S1). Immunocytochemistry for four TC proteins (NONO, YBX1, NPM1, and hnRNPC) confirmed the enrichment for NONO and YBX1 and interaction between NPM1-positive nucleoli and TCs (Figures 4H and 4I). hnRNPC was evenly distributed between TCs and nucleoplasm

Thus, TDP-43 sequestration into TCs leads to the loss of its soluble/diffuse pool and dissociation from its normal protein interactome. Given the low complexity of the TC proteome, functional inactivation of TDP-43 by sequestration may be the main, if not only, function of TCs.

# Stress-induced nuclear TDP-43 condensation elicits transient loss of function in splicing and prolonged STMN2 downregulation

Having demonstrated the loss of normal TDP-43 interactions due to its condensation during stress, we next examined the functional consequences of this molecular event using splicing as readout. SH-SY5Y cells were treated with NaAsO2 and left to recover for up to 6 h, and small interfering RNA (siRNA)-mediated TDP-43 knockdown was used in parallel as a positive control. This cell line was chosen due to high expression of STMN2, a well-characterized and ALS-relevant TDP-43 target.8 Efficient mounting of stress response was verified by measuring the expression of stress-inducible genes and eIF2α phosphorylation (Figures S8A and S8B). Exon 3 skipping in POLDIP3 and cryptic exon (CE) inclusion in EPB41L4A mRNAs, two well-known TDP-43 targets, were readily detectable as early as 1 h into the recovery (Figure 5A). These alternative splicing events persisted and became even more prominent at the later recovery time points (Figure 5A). We next quantified splicing changes in a panel of both well-established and recently reported<sup>50</sup> TDP-43 targets by RT-qPCR. We compared 1-h and 6-h recovery time points to selectively measure the effect of nuclear TDP-43 condensation, independent of its cytoplasmic relocalization, which occurs 1 h into the recovery. Out of six targets, four were found to have changed in the same direction as in TDP-43 siRNA-transfected

#### **Article**



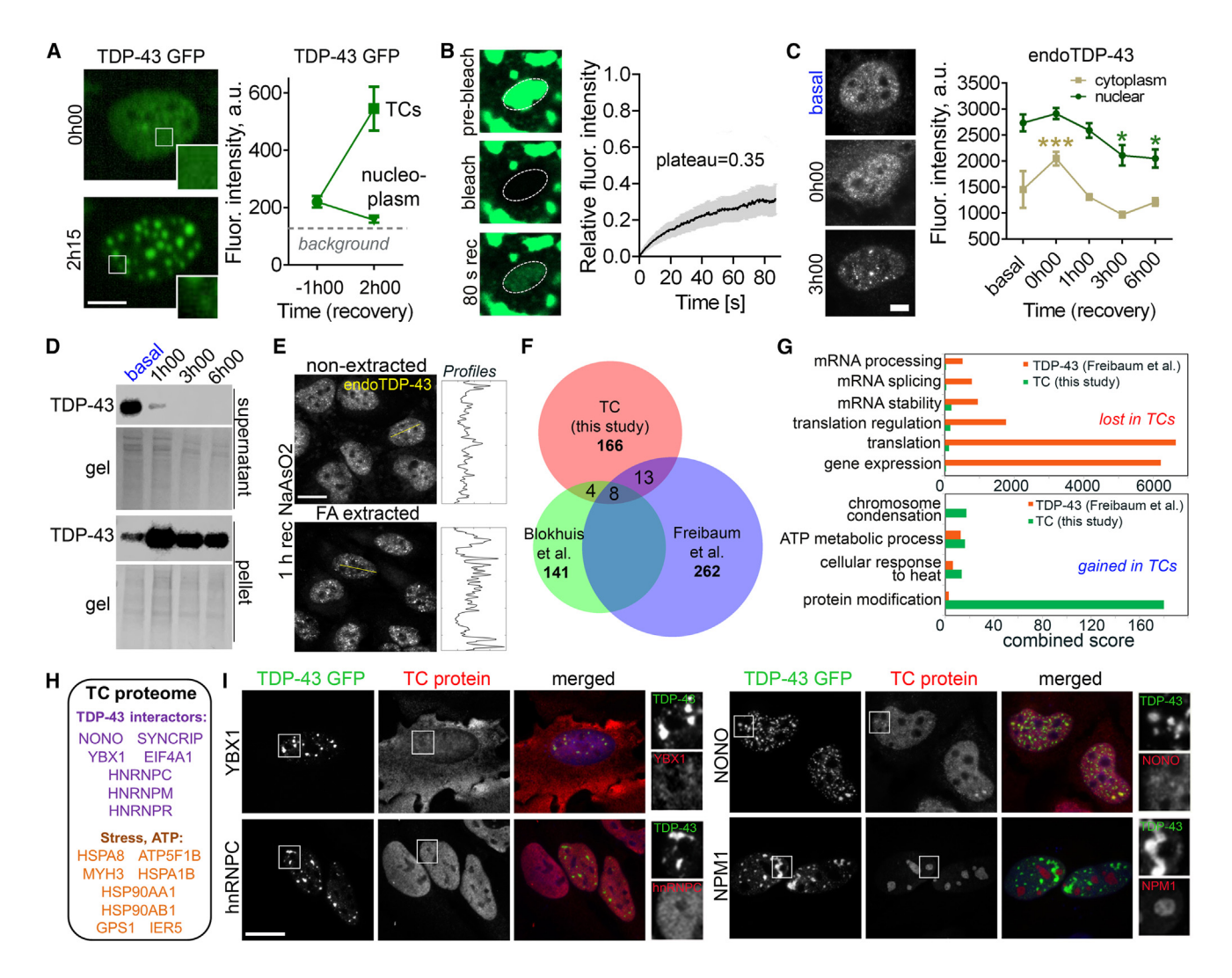


Figure 4. Stress-inducible TDP-43 condensation leads to its dissociation from the normal binding partners in the nucleus

- (A) Nucleoplasmic depletion of TDP-43 GFP upon TC assembly. Fluorescence intensity was analyzed in the center of TCs and in the inter-TC regions (nucleoplasm) before stress (–1h00) and 2 h into the recovery (38 and 27 cells, respectively, from nine fields of view). Scale bar, 5 μm.
- (B) FRAP analysis reveals inefficient fluorescence recovery after photobleaching of the entire TC. Ten cells (3 condensates in each nucleus) were analyzed.
- (C) Nuclear and cytoplasmic levels of soluble endogenous TDP-43 during recovery from stress. Fluorescence intensity was analyzed in ROIs selected in the cytoplasm and nucleus (outside TCs) of the same cell for  $\geq$  30 cells per time point from two independent experiments (N = 2). \*p < 0.05, \*\*\*p < 0.001, one-way ANOVA with Dunnett's post hoc test (nuclear) and unpaired t test (cytoplasmic). Scale bar, 5  $\mu$ m.
- (D) Reduced TDP-43 solubility during stress. Fractions were obtained by centrifugation in a detergent-containing buffer.
- (E) Early onset of TDP-43 condensation during the recovery from stress revealed by formamide extraction. Scale bar, 10 µm.
- (F and G) Proteomic analysis of purified TCs indicates their depletion of normal TDP-43 interactors. TCs formed by TDP-43 GFP were affinity purified as in Figure 2H. Analysis was done using two biological and two technical replicates. Two published TDP-43 interactomes were used for comparison (F), and enrichment of proteins within "biological process" GO terms, as compared to the normal TDP-43 interactome, was visualized (G). In (G),  $p_{adj}$  cutoff = 0.05; combined score is from Enrichr.

(H and I) TC proteins and their validation. Proteins common for the three datasets and TC proteins from stress response and ATP metabolism pathways are shown (H) alongside validation by immunocytochemistry (I). Scale bar, 10 μm.

In all panels, NaAsO<sub>2</sub> was used. In all cases, quantification data and/or images are from a representative experiment repeated three times (N = 3) unless indicated otherwise; number of technical replicates (fields of view, individual cells) is indicated for each panel.

cells, including a decrease in STMN2 mRNA (Figure 5B). *HDGFL2* (exon 5-containing isoform)<sup>51</sup> was not changed, and *NPHP4* had almost undetectable expression (data not shown). TDP-43 mRNA was also found to be upregulated (Figure 5B), consistent with the autoregulation mechanism.<sup>52</sup> STMN2 mRNA downregulation was due to CE inclusion, as confirmed

using primers detecting exon 2a-containing transcripts (Figure 5A). These changes were verified in hMNs at the 6-h recovery time point, at the onset of TC assembly (Figure 5C). Notably, STMN2 mRNA was downregulated by  $\sim$ 50%, accompanied by high levels of the CE-containing transcript, as early as the 1-h recovery time point (Figures 5C and 5D). Thus, nuclear TDP-43



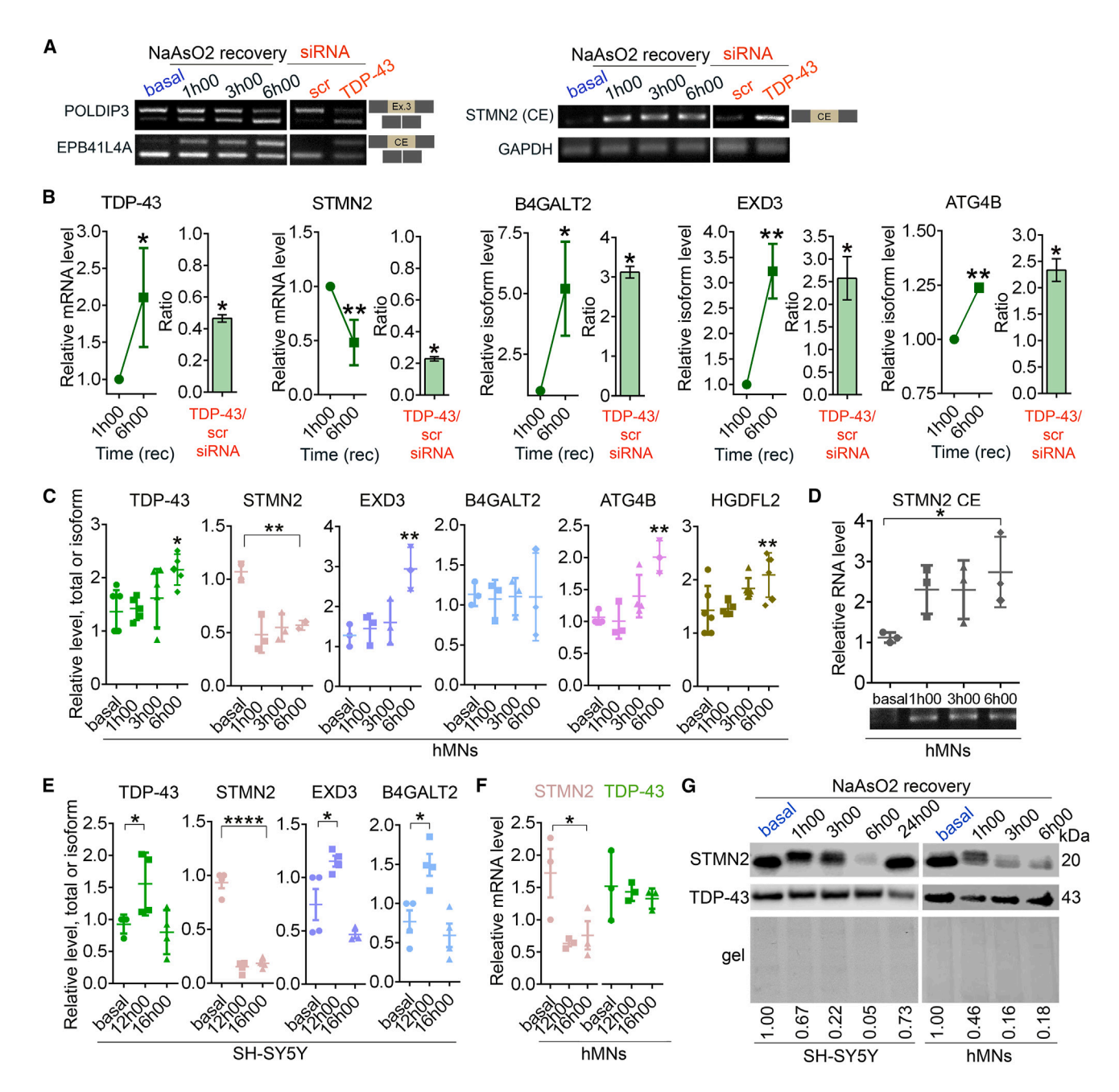


Figure 5. Stress-induced nuclear TDP-43 condensation leads to its loss of function in splicing and STMN2 depletion

(A and B) Splicing alterations induced by stress in SH-SY5Y cells are consistent with TDP-43 loss of function. Alternative splicing events were analyzed by PCR (A) or qPCR (B) during the recovery from NaAsO<sub>2</sub> stress. In (B), total mRNA levels were analyzed for STMN2 and TDP-43 and levels of alternative isoforms for other targets. For STMN2 cryptic exon (CE) analysis, primers specific to exon 2a-containing transcript were used. TDP-43 knockdown samples (48 h post transfection) were analyzed in parallel as a positive control. N = 3-5; \*p < 0.05, \*\*p < 0.05, \*\*p < 0.05, \*\*analyzed in parallel as a positive control.

- (C) Splicing alterations induced by stress in hMNs are consistent with TDP-43 loss of function. hMNs were analyzed by qPCR during recovery from NaAsO<sub>2</sub> stress. N = 3-6; \*p < 0.05, \*p < 0.05, \*p < 0.01, one-way ANOVA with Holm-Sidak post hoc test.
- (D) STMN2 CE inclusion during the recovery from NaAsO<sub>2</sub> stress in hMNs, as analyzed by PCR and qPCR using CE-specific primers. N = 3; \*p < 0.05, one-way ANOVA with Holm-Sidak test.
- (E and F) Slow recovery of STMN2 splicing in SH-SY5Y cells (E) and hMNs (F). Cells were analyzed by qPCR during recovery from NaAsO<sub>2</sub> stress. N = 4-5;  $^*p < 0.05$ ,  $^{****}p < 0.0001$ , one-way ANOVA with Holm-Sidak post hoc test. See also Figure S8C.
- (G) STMN2 protein depletion during the recovery from NaAsO<sub>2</sub> stress in SH-SY5Y cells and hMNs. Representative blots and quantification (mean values) are shown. N = 5 for SH-SY5Y cells and N = 2 for hMNs. See also Figures S8D and S8E.
- All RT-qPCR reactions included two technical replicates, and the number of biological replicates (N) is indicated for each panel.

#### **Article**



condensation is associated with splicing alterations of TDP-43 targets including *STMN2*.

TCs completely resolve by 16 h of recovery in SH-SY5Y cells (Figure S1C); however, unlike other TDP-43 targets, the STMN2 mRNA level did not recover by that time point (Figures 5E and S8C). STMN2 downregulation, but not TDP-43 upregulation, was also still detectable at this time point in hMNs (Figure 5F). At the protein level, we found prominent STMN2 depletion between 3 h and 6 h of recovery in both SH-SY5Y cells and hMNs, without changes in total TDP-43 (Figures 5G, S8D, and S8E). This effect was not due to cell toxicity/death, since it was fully reversible, with STMN2 protein level returning to the pre-stress/normal level by the 24-/30-h recovery time points (Figures 5G, S8D, and S8E). STMN2 is a short-lived protein (half-life ~2 h), 53,54 and we indeed observed its complete loss after 4 h of translational arrest with cycloheximide (Figure S8F). Interestingly, a change in STMN2 protein mobility was also observed early during stress (Figure 5G), potentially due to palmitoylation.<sup>54</sup> Thus, neuronal stress response is associated with long-lasting, but reversible, depletion of STMN2 (full-length) mRNA and protein.

#### **DISCUSSION**

Physiological condensates of TDP-43 characterized to date have been represented by RNA-rich assemblies; stress granules formed around mRNA, 15,55 paraspeckles nucleated by architectural NEAT1 RNA,28 small nuclear RNA-rich Cajal bodies,56 neuronal RNA transport granules,<sup>57</sup> myogranules containing sarcomeric protein-encoding mRNAs,30 and submicroscopic splicing condensates formed on UG-rich RNA.<sup>58</sup> In contrast. the two RNA-depleted TDP-43 assemblies described so far, aggresomes<sup>24,59</sup> and anisosomes,<sup>60</sup> demonstrate reduced dynamic properties and increased persistence and p62/ubiquitin accumulation and are often associated with cell death, suggesting their pathological nature. Furthermore, TDP-43 ALS-linked mutations<sup>61</sup> and its acetylation<sup>21</sup> can disrupt RNA binding. RNA was also found to neutralize toxic aggregated TDP-43 species in the cytoplasm.<sup>62</sup> Collectively, this body of knowledge suggested that TDP-43's loss of RNA binding and its incorporation into RNA-depleted structures equates with a pathological event. Here, we describe a TDP-43-rich RNA-depleted condensate with a physiological function: rapid and reversible TDP-43 inactivation during stress. It is important to note that being RNA depleted, TCs are not completely devoid of RNA and can recruit/sequester certain RNAs, for example, NEAT1.<sup>19</sup> Interestingly, although NEAT1 is dispensable for TC formation, it has a stabilizing effect on this assembly, 29 likely because of its unique properties as a long structured RNA densely coated with LCDcontaining proteins.<sup>28</sup>

Several types of non-liquid/non-dynamic functional condensates have been described.  $^{63}$  TCs display limited recovery in FRAP experiments, are stable in solution, are resistant to 1,6-hexanediol and mild detergents, and are detected by a  $\beta$ -sheet-specific antibody, suggesting that they are also non-LLPS assemblies. This physical state underlies efficient TDP-43 retention and, hence, functional inactivation during stress. Consistently, decreased TDP-43 mobility and solubility during stress were pre-

viously detected using a different set of approaches. 64,65 Condensates of TDP-43 and other RBPs can undergo transition from liquid-like to more solid (fibrilized, amyloid-like) state in vitro, and RNA serves as a chaperone increasing their liquid properties and limiting fibrilization. 40,66-68 TC formation is analogous to this transition, whereby TDP-43 loses association with dynamic, liquid-like RNP complexes and becomes embedded into a more stable, non-liquid assembly. Notably, sequestration of TDP-43 into reversible structures, nSBs, is also associated with loss of binding to  $\sim$ 80% of its RNA targets, <sup>16</sup> implicating similar assembly processes and condensate properties. TC dependence on ATP and enrichment in ATP-related factors suggest that TC assembly is an active and tightly regulated process rather than uncontrollable protein aggregation. Of note, ATP has been shown to modulate TDP-43 LLPS in vitro, 69 and relatively low ATP levels typical for neurons<sup>69</sup> may contribute to the slow TC assembly in this cell type. Several parallels can be drawn between TCs and stress granule cores, which are also relatively stable and involve ATP machinery.<sup>22</sup> Both structures are transient and fully resolve post stress, being physiological in their nature and cytoprotective under stress. 19,23,7

Using the CONA assay, we found that the M337V variant decreases and D169G increases TDP-43 concentration on UG-RNA-coated beads. This result can be interpreted as reduced and augmented capacity of M337V and D169G variants, respectively, to generate/enter the LLPS RNP "shell" formed on the bead. An antagonism between (RNA-nucleated) LLPS of TDP-43 and its fibrilization have been reported. 40,71 Indeed, M337V affects an  $\alpha$ -helical segment in the CTD and disrupts TDP-43 LLPS in vitro and in unstressed cells, promoting conversion into a fibrilized state. 40,44 On the other hand, the D169G variant was found to be resistant to fibrilization in vitro.72 Of note, D169G was previously found to disrupt ATP binding, 73 which may also contribute to its effect on TC assembly. Our version of CONA is not a simple RNA-binding assay but rather an "RNP incorporation" assav, since it uses whole-cell lysates rich in RNA and numerous RBPs that will modulate TDP-43 interactions. The assay is useful for detecting subtle changes in TDP-43's capability to assemble/enter RNPs in a complex molecular environment close to cellular. Overall, our finding that different ALS-causative mutations can affect TDP-43 condensation in opposite directions emphasizes the importance of optimal TDP-43 condensation properties for neuronal homeostasis.

TDP-43 loss of function leads to widespread splicing alterations in its target genes, of which hundreds are currently known. <sup>36,74,75</sup> We find that cellular stress induces a TDP-43 loss-of-function splicing signature due to its depletion via nuclear condensation. Consistently, in a recent report, a stress-inducing drug led to splicing changes consistent with TDP-43 loss of function. <sup>76</sup> Altered splicing of some TDP-43 target genes, e.g., *STMN2* and *UNC13A*, results in protein depletion, which can lead to neuronal dysfunction such as axonal abnormalities. <sup>8,9,50,77-79</sup> In addition, novel protein isoforms can be produced from the differentially spliced transcripts, <sup>80</sup> which may exert unwanted and even toxic effects on neurons. Therefore, a physiological benefit of TDP-43 (splicing) loss of function in stressed neurons is not obvious at first sight. However, firstly, the changes elicited by TCs are transient: even with the relatively





severe arsenite-induced stress, normal splicing patterns are largely restored after 16 h of recovery. Secondly, most novel mRNA isoforms generated through cryptic/skiptic events may be short-lived and not give rise to substantial amounts of deleterious protein variants. Alternatively, novel protein or RNA isoforms may be neutral or may have a cytoprotective effect. In addition, transient depletion of certain proteins may be beneficial in stressed neurons. For example, STMN2 is a microtubule-destabilizing protein, and its upregulation was found to mediate neurotoxicity in an ALS-SOD1 mouse model.81 Thus, its acute downregulation during stress may have a protective effect on the cytoskeleton. However, repetitive or chronic stress or ALS mutations perturbing TC homeostasis will lead to recurrent/persisting changes in splicing, and the slowly recovering targets, such as STMN2, will be disproportionately affected. Constitutive loss of STMN2 causes motor neuropathy in mouse models. 10,82 Determining short-term vs. long-term effects of STMN2 depletion, including under stress, should help establish a safe window for its therapeutic modulation in ALS. It would be also important to identify other TDP-43 splicing targets with slow recovery rates and, hence, high sensitivity to chronic stress. Interestingly, in our recent study, we observed abnormal nuclear TDP-43 condensation in an optogenetic model of C9orf72-induced pathology.83 Supporting our cellular data, a recent study in postmortem tissue has reported nuclear TDP-43 granulation correlating with STMN2-CE transcript accumulation in ALS spinal motor neurons.84 Therapies directed at the optimization of cellular stress response may be of promise in ALS treatment.

#### **Limitations of the study**

A chemical stress was used throughout the study to induce TDP-43 condensation. More physiological stressors should be used in the future, including in *in vivo* models. A single type of TDP-43 target RNA sequence (pure UG repeats) and relatively short RNA oligonucleotides were used in this work, whereas TDP-43 binds to a repertoire of UG-rich sequences. The main limitation of the CONA assay is that the subcellular protein compartmentalization is lost after cell lysis. Nevertheless, the assay bridges the gap between oligo-component *in vitro* assays with purified protein and cellular assays.

#### STAR\*METHODS

Detailed methods are provided in the online version of this paper and include the following:

- KEY RESOURCES TABLE
- RESOURCE AVAILABILITY
  - Lead contact
  - Materials availability
  - Data and code availability
- EXPERIMENTAL MODEL AND STUDY PARTICIPANT DETAILS
  - Cell lines
- Human tissue
- METHOD DETAILS
  - o Plasmids
  - Cell transfection and treatment
  - o Immunofluorescence
  - $\,\circ\,$  Cell microscopy and quantification
  - $\circ \ \ \mathsf{FRAP} \ \mathsf{analysis}$
  - RNA expression analysis

- o TDP-43 solubility analysis and western blotting
- o TDP-43 condensate isolation and stability analysis
- O TDP-43 condensate proteomic analysis
- Soluble TDP-43 interactome analysis
- Confocal nanoscanning (CONA)
- o In vitro analysis of recombinant TDP-43 assemblies
- Immunohistochemistry
- QUANTIFICATION AND STATISTICAL ANALYSIS
  - o Mass spectrometry data processing
  - Statistical analysis

#### SUPPLEMENTAL INFORMATION

Supplemental information can be found online at https://doi.org/10.1016/j.ceirep.2024.114421.

#### **ACKNOWLEDGMENTS**

The work was supported by UKRI Future Leaders Fellowship (MR/W004615/1), MRC (MR/W028522/1), and BBSRC (BB/V014110/1) grants, MND Association grant (Shelkovnikova/Oct17/968-799), and MRC grant (MR/X012077/1) for Airyscan 2 LMF. B.C.S.E. is supported by an MND Scotland PhD studentship (to T.A.S.). T.M. is funded by an MND Association junior non-clinical fellowship (2323-799). We acknowledge the London Neurodegenerative Diseases Brain Bank for providing human tissue and Adrian Higginbottom for assisting with CONA automated quantification pipeline development.

#### **AUTHOR CONTRIBUTIONS**

T.A.S. conceived and designed the study, conducted experiments (conventional imaging, high-content imaging, compound treatment, and fractionation), analyzed data, supervised the study, and wrote the manuscript. W.-P.H. generated genetic constructs, developed and applied the CONA assay, and performed *in vitro* experiments and western blots. B.C.S.E. performed neuronal and astrocyte differentiation, cellular stress experiments, splicing analysis (PCR and qPCR), and western blots. R.E.H. performed TC purification, SRM, and FRAP analysis. A.S.A. conducted immunohistochemistry and proteomic dataset analysis. V.K. and J.R. assisted with stress experiments and related quantification. T.M. assisted with neuronal differentiation. All authors analyzed data, contributed to manuscript writing, and approved its final version.

#### DECLARATION OF INTERESTS

The authors declare no competing interests.

Received: January 10, 2024 Revised: April 4, 2024 Accepted: June 14, 2024 Published: June 27, 2024

#### REFERENCES

- Tziortzouda, P., Van Den Bosch, L., and Hirth, F. (2021). Triad of TDP43 control in neurodegeneration: autoregulation, localization and aggregation. Nat. Rev. Neurosci. 22, 197–208. https://doi.org/10.1038/s41583-021-00431-1.
- Arai, T., Hasegawa, M., Akiyama, H., Ikeda, K., Nonaka, T., Mori, H., Mann, D., Tsuchiya, K., Yoshida, M., Hashizume, Y., and Oda, T. (2006). TDP-43 is a component of ubiquitin-positive tau-negative inclusions in frontotemporal lobar degeneration and amyotrophic lateral sclerosis. Biochem. Biophys. Res. Commun. 351, 602–611. https://doi.org/10.1016/j.bbrc.2006.
- Neumann, M., Sampathu, D.M., Kwong, L.K., Truax, A.C., Micsenyi, M.C., Chou, T.T., Bruce, J., Schuck, T., Grossman, M., Clark, C.M., et al. (2006). Ubiquitinated TDP-43 in frontotemporal lobar degeneration and

#### **Article**



- amyotrophic lateral sclerosis. Science 314, 130–133. https://doi.org/10.1126/science.1134108.
- Lattante, S., Rouleau, G.A., and Kabashi, E. (2013). TARDBP and FUS mutations associated with amyotrophic lateral sclerosis: summary and update. Hum. Mutat. 34, 812–826. https://doi.org/10.1002/humu.22319.
- Sreedharan, J., Blair, I.P., Tripathi, V.B., Hu, X., Vance, C., Rogelj, B., Ackerley, S., Durnall, J.C., Williams, K.L., Buratti, E., et al. (2008). TDP-43 mutations in familial and sporadic amyotrophic lateral sclerosis. Science 319, 1668–1672. https://doi.org/10.1126/science.1154584.
- de Boer, E.M.J., Orie, V.K., Williams, T., Baker, M.R., De Oliveira, H.M., Polvikoski, T., Silsby, M., Menon, P., van den Bos, M., Halliday, G.M., et al. (2020). TDP-43 proteinopathies: a new wave of neurodegenerative diseases. J. Neurol. Neurosurg. Psychiatry 92, 86–95. https://doi.org/10. 1136/jnnp-2020-322983.
- Ratti, A., and Buratti, E. (2016). Physiological Functions and Pathobiology of TDP-43 and FUS/TLS proteins. J. Neurochem. 138, 95–111. https://doi. org/10.1111/inc.13625.
- Melamed, Z., López-Erauskin, J., Baughn, M.W., Zhang, O., Drenner, K., Sun, Y., Freyermuth, F., McMahon, M.A., Beccari, M.S., Artates, J.W., et al. (2019). Premature polyadenylation-mediated loss of stathmin-2 is a hallmark of TDP-43-dependent neurodegeneration. Nat. Neurosci. 22, 180–190. https://doi.org/10.1038/s41593-018-0293-z.
- Klim, J.R., Williams, L.A., Limone, F., Guerra San Juan, I., Davis-Dusenbery, B.N., Mordes, D.A., Burberry, A., Steinbaugh, M.J., Gamage, K.K., Kirchner, R., et al. (2019). ALS-implicated protein TDP-43 sustains levels of STMN2, a mediator of motor neuron growth and repair. Nat. Neurosci. 22, 167–179. https://doi.org/10.1038/s41593-018-0300-4.
- Lopez-Erauskin, J., Bravo-Hernandez, M., Presa, M., Baughn, M.W., Melamed, Z., Beccari, M.S., Agra de Almeida Quadros, A.R., Arnold-Garcia, O., Zuberi, A., Ling, K., et al. (2023). Stathmin-2 loss leads to neurofilament-dependent axonal collapse driving motor and sensory denervation. Nat. Neurosci. 27, 34–47. https://doi.org/10.1038/s41593-023-01496-0.
- Fakim, H., and Vande Velde, C. (2024). The implications of physiological biomolecular condensates in amyotrophic lateral sclerosis. Semin. Cell Dev. Biol. 156, 176–189. https://doi.org/10.1016/j.semcdb.2023.05.006.
- Afroz, T., Hock, E.M., Ernst, P., Foglieni, C., Jambeau, M., Gilhespy, L.A.B., Laferriere, F., Maniecka, Z., Plückthun, A., Mittl, P., et al. (2017). Functional and dynamic polymerization of the ALS-linked protein TDP-43 antagonizes its pathologic aggregation. Nat. Commun. 8, 45. https:// doi.org/10.1038/s41467-017-00062-0.
- Chang, C.K., Wu, T.H., Wu, C.Y., Chiang, M.H., Toh, E.K.W., Hsu, Y.C., Lin, K.F., Liao, Y.H., Huang, T.H., and Huang, J.J.T. (2012). The N-terminus of TDP-43 promotes its oligomerization and enhances DNA binding affinity. Biochem. Biophys. Res. Commun. 425, 219–224. https://doi.org/10.1016/j.bbrc.2012.07.071.
- An, H., de Meritens, C.R., and Shelkovnikova, T.A. (2021). Connecting the "dots": RNP granule network in health and disease. Biochim. Biophys. Acta Mol. Cell Res. 1868, 119058. https://doi.org/10.1016/j.bbamcr. 2021.119058.
- Colombrita, C., Zennaro, E., Fallini, C., Weber, M., Sommacal, A., Buratti, E., Silani, V., and Ratti, A. (2009). TDP-43 is recruited to stress granules in conditions of oxidative insult. J. Neurochem. 111, 1051–1061. https://doi. org/10.1111/j.1471-4159.2009.06383.x.
- Udan-Johns, M., Bengoechea, R., Bell, S., Shao, J., Diamond, M.I., True, H.L., Weihl, C.C., and Baloh, R.H. (2014). Prion-like nuclear aggregation of TDP-43 during heat shock is regulated by HSP40/70 chaperones. Hum. Mol. Genet. 23, 157–170. https://doi.org/10.1093/hmg/ddt408.
- Jung, K.H., Sun, J., Hsiung, C.H., Lance Lian, X., Liu, Y., and Zhang, X. (2023). Nuclear bodies protect phase separated proteins from degradation in stressed proteome. Preprint at bioRxiv. https://doi.org/10.1101/2023.04.19.537522.
- Gerovska, D., Irizar, H., Otaegi, D., Ferrer, I., López de Munain, A., and Araúzo-Bravo, M.J. (2020). Genealogy of the neurodegenerative diseases

- based on a meta-analysis of age-stratified incidence data. Sci. Rep. 10, 18923. https://doi.org/10.1038/s41598-020-75014-8.
- Wang, C., Duan, Y., Duan, G., Wang, Q., Zhang, K., Deng, X., Qian, B., Gu, J., Ma, Z., Zhang, S., et al. (2020). Stress Induces Dynamic, Cytotoxicity-Antagonizing TDP-43 Nuclear Bodies via Paraspeckle LncRNA NEAT1-Mediated Liquid-Liquid Phase Separation. Mol. Cell 79, 443–458.e7. https://doi.org/10.1016/j.molcel.2020.06.019.
- Gruijs da Silva, L.A., Simonetti, F., Hutten, S., Riemenschneider, H., Sternburg, E.L., Pietrek, L.M., Gebel, J., Dötsch, V., Edbauer, D., Hummer, G., et al. (2022). Disease-linked TDP-43 hyperphosphorylation suppresses TDP-43 condensation and aggregation. EMBO J. 41, e108443. https://doi.org/10.15252/embj.2021108443.
- Cohen, T.J., Hwang, A.W., Restrepo, C.R., Yuan, C.X., Trojanowski, J.Q., and Lee, V.M.Y. (2015). An acetylation switch controls TDP-43 function and aggregation propensity. Nat. Commun. 6, 5845. https://doi.org/10. 1038/ncomms6845.
- Jain, S., Wheeler, J.R., Walters, R.W., Agrawal, A., Barsic, A., and Parker, R. (2016). ATPase-Modulated Stress Granules Contain a Diverse Proteome and Substructure. Cell 164, 487–498. https://doi.org/10.1016/j.cell. 2015.12.038.
- Shelkovnikova, T.A., Dimasi, P., Kukharsky, M.S., An, H., Quintiero, A., Schirmer, C., Buée, L., Galas, M.C., and Buchman, V.L. (2017). Chronically stressed or stress-preconditioned neurons fail to maintain stress granule assembly. Cell Death Dis. 8, e2788. https://doi.org/10.1038/cddis. 2017.199.
- Perez-Berlanga, M., Wiersma, V.I., Zbinden, A., De Vos, L., Wagner, U., Foglieni, C., Mallona, I., Betz, K.M., Clery, A., Weber, J., et al. (2023). Loss of TDP-43 oligomerization or RNA binding elicits distinct aggregation patterns. EMBO J. 42, e111719. https://doi.org/10.15252/embj. 2022111719.
- Collins, M., Li, Y., and Bowser, R. (2020). RBM45 associates with nuclear stress bodies and forms nuclear inclusions during chronic cellular stress and in neurodegenerative diseases. Acta Neuropathol. Commun. 8, 91. https://doi.org/10.1186/s40478-020-00965-y.
- Tsuiji, H., Iguchi, Y., Furuya, A., Kataoka, A., Hatsuta, H., Atsuta, N., Tanaka, F., Hashizume, Y., Akatsu, H., Murayama, S., et al. (2013). Spliceosome integrity is defective in the motor neuron diseases ALS and SMA. EMBO Mol. Med. 5, 221–234. https://doi.org/10.1002/emmm.201202303.
- Modic, M., Grosch, M., Rot, G., Schirge, S., Lepko, T., Yamazaki, T., Lee, F.C.Y., Rusha, E., Shaposhnikov, D., Palo, M., et al. (2019). Cross-Regulation between TDP-43 and Paraspeckles Promotes Pluripotency-Differentiation Transition. Mol. Cell 74, 951–965.e13. https://doi.org/10.1016/j.molcel.2019.03.041.
- West, J.A., Mito, M., Kurosaka, S., Takumi, T., Tanegashima, C., Chujo, T., Yanaka, K., Kingston, R.E., Hirose, T., Bond, C., et al. (2016). Structural, super-resolution microscopy analysis of paraspeckle nuclear body organization. J. Cell Biol. 214, 817–830. https://doi.org/10.1083/jcb.201601071.
- Hodgson, R., Huang, W.-P., Kumar, V., An, H., Chalakova, Z., Rayment, J., Ellis, B.C., Stender, E.G., van Vugt, J.J., Sequencing Consortium, P.M.A., et al. (2024). TDP-43 is a Master Regulator of Paraspeckle Condensation. SSRN. https://doi.org/10.2139/ssrn.4721338.
- Vogler, T.O., Wheeler, J.R., Nguyen, E.D., Hughes, M.P., Britson, K.A., Lester, E., Rao, B., Betta, N.D., Whitney, O.N., Ewachiw, T.E., et al. (2018). TDP-43 and RNA form amyloid-like myo-granules in regenerating muscle. Nature 563, 508–513. https://doi.org/10.1038/s41586-018-0665-2.
- Kayed, R., Head, E., Thompson, J.L., McIntire, T.M., Milton, S.C., Cotman, C.W., and Glabe, C.G. (2003). Common structure of soluble amyloid oligomers implies common mechanism of pathogenesis. Science 300, 486–489. https://doi.org/10.1126/science.1079469.
- Oiwa, K., Watanabe, S., Onodera, K., Iguchi, Y., Kinoshita, Y., Komine, O., Sobue, A., Okada, Y., Katsuno, M., and Yamanaka, K. (2023). Monomerization of TDP-43 is a key determinant for inducing TDP-43 pathology in





- amyotrophic lateral sclerosis. Sci. Adv. 9, eadf6895. https://doi.org/10. 1126/sciadv.adf6895.
- Zhang, Y.J., Caulfield, T., Xu, Y.F., Gendron, T.F., Hubbard, J., Stetler, C., Sasaguri, H., Whitelaw, E.C., Cai, S., Lee, W.C., and Petrucelli, L. (2013). The dual functions of the extreme N-terminus of TDP-43 in regulating its biological activity and inclusion formation. Hum. Mol. Genet. 22, 3112– 3122. https://doi.org/10.1093/hmg/ddt166.
- Tsoi, P.S., Choi, K.J., Leonard, P.G., Sizovs, A., Moosa, M.M., MacKenzie, K.R., Ferreon, J.C., and Ferreon, A.C.M. (2017). The N-Terminal Domain of ALS-Linked TDP-43 Assembles without Misfolding. Angew Chem. Int. Ed. Engl. 56, 12590–12593. https://doi.org/10.1002/anie.201706769.
- Stanek, D., and Fox, A.H. (2017). Nuclear bodies: news insights into structure and function. Curr. Opin. Cell Biol. 46, 94–101. https://doi.org/10.1016/j.ceb.2017.05.001.
- Tollervey, J.R., Curk, T., Rogelj, B., Briese, M., Cereda, M., Kayikci, M., König, J., Hortobágyi, T., Nishimura, A.L., Zupunski, V., et al. (2011). Characterizing the RNA targets and position-dependent splicing regulation by TDP-43. Nat. Neurosci. 14, 452–458. https://doi.org/10.1038/nn.2778.
- Ederle, H., Funk, C., Abou-Ajram, C., Hutten, S., Funk, E.B.E., Kehlenbach, R.H., Bailer, S.M., and Dormann, D. (2018). Nuclear egress of TDP-43 and FUS occurs independently of Exportin-1/CRM1. Sci. Rep. 8, 7084. https://doi.org/10.1038/s41598-018-25007-5.
- Buratti, E., Dörk, T., Zuccato, E., Pagani, F., Romano, M., and Baralle, F.E. (2001). Nuclear factor TDP-43 and SR proteins promote in vitro and in vivo CFTR exon 9 skipping. EMBO J. 20, 1774–1784. https://doi.org/10.1093/ emboj/20.7.1774.
- Kedersha, N.L., Gupta, M., Li, W., Miller, I., and Anderson, P. (1999). RNA-binding proteins TIA-1 and TIAR link the phosphorylation of eIF-2 alpha to the assembly of mammalian stress granules. J. Cell Biol. 147, 1431–1442. https://doi.org/10.1083/jcb.147.7.1431.
- Grese, Z.R., Bastos, A.C., Mamede, L.D., French, R.L., Miller, T.M., and Ayala, Y.M. (2021). Specific RNA interactions promote TDP-43 multivalent phase separation and maintain liquid properties. EMBO Rep. 22, e53632. https://doi.org/10.15252/embr.202153632.
- An, H., Tan, J.T., and Shelkovnikova, T.A. (2019). Stress granules regulate stress-induced paraspeckle assembly. J. Cell Biol. 218, 4127–4140. https://doi.org/10.1083/jcb.201904098.
- Cooper-Knock, J., Julian, T.H., Feneberg, E., Highley, J.R., Sidra, M., Turner, M.R., Talbot, K., Ansorge, O., Allen, S.P., Moll, T., et al. (2023). Atypical TDP-43 protein expression in an ALS pedigree carrying a p.Y374X truncation mutation in TARDBP. Brain Pathol. 33, e13104. https://doi.org/10.1111/bpa.13104.
- Chiang, C.H., Grauffel, C., Wu, L.S., Kuo, P.H., Doudeva, L.G., Lim, C., Shen, C.K.J., and Yuan, H.S. (2016). Structural analysis of disease-related TDP-43 D169G mutation: linking enhanced stability and caspase cleavage efficiency to protein accumulation. Sci. Rep. 6, 21581. https://doi.org/10. 1038/srep21581.
- Conicella, A.E., Zerze, G.H., Mittal, J., and Fawzi, N.L. (2016). ALS Mutations Disrupt Phase Separation Mediated by alpha-Helical Structure in the TDP-43 Low-Complexity C-Terminal Domain. Structure 24, 1537–1549. https://doi.org/10.1016/j.str.2016.07.007.
- Zhu, S., Choudhury, N.R., Rooney, S., Pham, N.T., Koszela, J., Kelly, D., Spanos, C., Rappsilber, J., Auer, M., and Michlewski, G. (2021). RNA pull-down confocal nanoscanning (RP-CONA) detects quercetin as primiR-7/HuR interaction inhibitor that decreases alpha-synuclein levels. Nucleic Acids Res. 49, 6456–6473. https://doi.org/10.1093/nar/gkab484.
- Duan, L., Zaepfel, B.L., Aksenova, V., Dasso, M., Rothstein, J.D., Kalab, P., and Hayes, L.R. (2022). Nuclear RNA binding regulates TDP-43 nuclear localization and passive nuclear export. Cell Rep. 40, 111106. https://doi. org/10.1016/j.celrep.2022.111106.
- Dos Passos, P.M., Hemamali, E.H., Mamede, L.D., Hayes, L.R., and Ayala, Y.M. (2023). RNA-mediated ribonucleoprotein assembly controls TDP-43

- nuclear retention. Preprint at bioRxiv. https://doi.org/10.1101/2023.08.06. 552215.
- Blokhuis, A.M., Koppers, M., Groen, E.J.N., van den Heuvel, D.M.A., Dini Modigliani, S., Anink, J.J., Fumoto, K., van Diggelen, F., Snelting, A., Sodaar, P., et al. (2016). Comparative interactomics analysis of different ALS-associated proteins identifies converging molecular pathways. Acta Neuropathol. 132, 175–196. https://doi.org/10.1007/s00401-016-1575-8.
- Freibaum, B.D., Chitta, R.K., High, A.A., and Taylor, J.P. (2010). Global analysis of TDP-43 interacting proteins reveals strong association with RNA splicing and translation machinery. J. Proteome Res. 9, 1104– 1120. https://doi.org/10.1021/pr901076y.
- Cao, M.C., Ryan, B., Wu, J., Curtis, M.A., Faull, R.L.M., Dragunow, M., and Scotter, E.L. (2023). A panel of TDP-43-regulated splicing events verifies loss of TDP-43 function in amyotrophic lateral sclerosis brain tissue. Neurobiol. Dis. 185, 106245. https://doi.org/10.1016/j.nbd.2023.106245.
- Irwin, K.E., Jasin, P., Braunstein, K.E., Sinha, I.R., Garret, M.A., Bowden, K.D., Chang, K., Troncoso, J.C., Moghekar, A., Oh, E.S., et al. (2024). A fluid biomarker reveals loss of TDP-43 splicing repression in presymptomatic ALS-FTD. Nat. Med. 30, 382–393. https://doi.org/10.1038/s41591-023-02788-5.
- Polymenidou, M., Lagier-Tourenne, C., Hutt, K.R., Huelga, S.C., Moran, J., Liang, T.Y., Ling, S.C., Sun, E., Wancewicz, E., Mazur, C., et al. (2011). Long pre-mRNA depletion and RNA missplicing contribute to neuronal vulnerability from loss of TDP-43. Nat. Neurosci. 14, 459–468. https:// doi.org/10.1038/nn.2779.
- Shin, J.E., Miller, B.R., Babetto, E., Cho, Y., Sasaki, Y., Qayum, S., Russler, E.V., Cavalli, V., Milbrandt, J., and DiAntonio, A. (2012). SCG10 is a JNK target in the axonal degeneration pathway. Proc. Natl. Acad. Sci. USA 109, E3696–E3705. https://doi.org/10.1073/pnas.1216204109.
- Thornburg-Suresh, E.J.C., Richardson, J.E., and Summers, D.W. (2023).
   The Stathmin-2 membrane-targeting domain is required for axon protection and regulated degradation by DLK signaling. J. Biol. Chem. 299, 104861. https://doi.org/10.1016/j.jbc.2023.104861.
- McDonald, K.K., Aulas, A., Destroismaisons, L., Pickles, S., Beleac, E., Camu, W., Rouleau, G.A., and Vande Velde, C. (2011). TAR DNA-binding protein 43 (TDP-43) regulates stress granule dynamics via differential regulation of G3BP and TIA-1. Hum. Mol. Genet. 20, 1400–1410. https:// doi.org/10.1093/hmg/ddr021.
- 56. Izumikawa, K., Nobe, Y., Ishikawa, H., Yamauchi, Y., Taoka, M., Sato, K., Nakayama, H., Simpson, R.J., Isobe, T., and Takahashi, N. (2019). TDP-43 regulates site-specific 2'-O-methylation of U1 and U2 snRNAs via controlling the Cajal body localization of a subset of C/D scaRNAs. Nucleic Acids Res. 47, 2487–2505. https://doi.org/10.1093/nar/gkz086.
- Alami, N.H., Smith, R.B., Carrasco, M.A., Williams, L.A., Winborn, C.S., Han, S.S.W., Kiskinis, E., Winborn, B., Freibaum, B.D., Kanagaraj, A., et al. (2014). Axonal transport of TDP-43 mRNA granules is impaired by ALS-causing mutations. Neuron 81, 536–543. https://doi.org/10.1016/j. neuron.2013.12.018.
- Hallegger, M., Chakrabarti, A.M., Lee, F.C.Y., Lee, B.L., Amalietti, A.G., Odeh, H.M., Copley, K.E., Rubien, J.D., Portz, B., Kuret, K., et al. (2021).
   TDP-43 condensation properties specify its RNA-binding and regulatory repertoire. Cell 184, 4680–4696.e22. https://doi.org/10.1016/j.cell.2021.
- Watanabe, S., Inami, H., Oiwa, K., Murata, Y., Sakai, S., Komine, O., Sobue, A., Iguchi, Y., Katsuno, M., and Yamanaka, K. (2020). Aggresome formation and liquid-liquid phase separation independently induce cytoplasmic aggregation of TAR DNA-binding protein 43. Cell Death Dis. 11, 909. https://doi.org/10.1038/s41419-020-03116-2.
- Yu, H., Lu, S., Gasior, K., Singh, D., Vazquez-Sanchez, S., Tapia, O., Toprani, D., Beccari, M.S., Yates, J.R., 3rd, Da Cruz, S., et al. (2021). HSP70 chaperones RNA-free TDP-43 into anisotropic intranuclear liquid spherical shells. Science 371, eabb4309. https://doi.org/10.1126/science.abb4309.
- Chen, H.J., Topp, S.D., Hui, H.S., Zacco, E., Katarya, M., McLoughlin, C., King, A., Smith, B.N., Troakes, C., Pastore, A., and Shaw, C.E. (2019).

#### **Article**



- RRM adjacent TARDBP mutations disrupt RNA binding and enhance TDP-43 proteinopathy. Brain *142*, 3753–3770. https://doi.org/10.1093/brain/awz313.
- Mann, J.R., Gleixner, A.M., Mauna, J.C., Gomes, E., DeChellis-Marks, M.R., Needham, P.G., Copley, K.E., Hurtle, B., Portz, B., Pyles, N.J., et al. (2019). RNA Binding Antagonizes Neurotoxic Phase Transitions of TDP-43. Neuron 102, 321–338.e8. https://doi.org/10.1016/j.neuron. 2019.01.048.
- 63. Woodruff, J.B., Hyman, A.A., and Boke, E. (2018). Organization and Function of Non-dynamic Biomolecular Condensates. Trends Biochem. Sci. 43, 81–94. https://doi.org/10.1016/j.tibs.2017.11.005.
- Streit, L., Kuhn, T., Vomhof, T., Bopp, V., Ludolph, A.C., Weishaupt, J.H., Gebhardt, J.C.M., Michaelis, J., and Danzer, K.M. (2022). Stress induced TDP-43 mobility loss independent of stress granules. Nat. Commun. 13, 5480. https://doi.org/10.1038/s41467-022-32939-0.
- French, R.L., Grese, Z.R., Aligireddy, H., Dhavale, D.D., Reeb, A.N., Kedia, N., Kotzbauer, P.T., Bieschke, J., and Ayala, Y.M. (2019). Detection of TAR DNA-binding protein 43 (TDP-43) oligomers as initial intermediate species during aggregate formation. J. Biol. Chem. 294, 6696–6709. https://doi. org/10.1074/jbc.RA118.005889.
- Peskett, T.R., Rau, F., O'Driscoll, J., Patani, R., Lowe, A.R., and Saibil, H.R. (2018). A Liquid to Solid Phase Transition Underlying Pathological Huntingtin Exon1 Aggregation. Mol. Cell 70, 588–601.e6. https://doi.org/ 10.1016/j.molcel.2018.04.007.
- 67. Rengifo-Gonzalez, J.C., El Hage, K., Clément, M.J., Steiner, E., Joshi, V., Craveur, P., Durand, D., Pastré, D., and Bouhss, A. (2021). The cooperative binding of TDP-43 to GU-rich RNA repeats antagonizes TDP-43 aggregation. Elife 10, e67605. https://doi.org/10.7554/eLife.67605.
- Sun, Y., Arslan, P.E., Won, A., Yip, C.M., and Chakrabartty, A. (2014).
   Binding of TDP-43 to the 3'UTR of its cognate mRNA enhances its solubility. Biochemistry 53, 5885–5894. https://doi.org/10.1021/bi500617x.
- Dang, M., Lim, L., Kang, J., and Song, J. (2021). ATP biphasically modulates LLPS of TDP-43 PLD by specifically binding arginine residues. Commun. Biol. 4, 714. https://doi.org/10.1038/s42003-021-02247-2.
- Glineburg, M.R., Yildirim, E., Gomez, N., Li, X., Pak, J., Altheim, C., Waksmacki, J., McInerney, G., Barmada, S.J., and Todd, P.K. (2023). Stress granule formation helps to mitigate neurodegeneration. Preprint at bio-Rxiv. https://doi.org/10.1101/2023.11.07.566060.
- Scherer, N.M., Maurel, C., Graus, M.S., McAlary, L., Richter, G., Radford, R.A.W., Hogan, A., Don, E.K., Lee, A., Yerbury, J., et al. (2024). RNA-binding properties orchestrate TDP-43 homeostasis through condensate formation in vivo. Nucleic Acids Res. 52, 5301–5319. https://doi.org/10. 1093/nar/gkae112.
- Austin, J.A., Wright, G.S.A., Watanabe, S., Grossmann, J.G., Antonyuk, S.V., Yamanaka, K., and Hasnain, S.S. (2014). Disease causing mutants of TDP-43 nucleic acid binding domains are resistant to aggregation and have increased stability and half-life. Proc. Natl. Acad. Sci. USA 111, 4309–4314. https://doi.org/10.1073/pnas.1317317111.
- Dang, M., and Song, J. (2020). ALS-causing D169G mutation disrupts the ATP-binding capacity of TDP-43 RRM1 domain. Biochem. Biophys. Res. Commun. 524, 459–464. https://doi.org/10.1016/j.bbrc.2020.01.122.
- Ling, J.P., Pletnikova, O., Troncoso, J.C., and Wong, P.C. (2015). TDP-43 repression of nonconserved cryptic exons is compromised in ALS-FTD. Science 349, 650–655. https://doi.org/10.1126/science.aab0983.
- De Conti, L., Akinyi, M.V., Mendoza-Maldonado, R., Romano, M., Baralle, M., and Buratti, E. (2015). TDP-43 affects splicing profiles and isoform production of genes involved in the apoptotic and mitotic cellular pathways. Nucleic Acids Res. 43, 8990–9005. https://doi.org/10.1093/nar/gkv814.
- Sinha, I.R., Sandal, P.S., Burns, G.D., Mallika, A.P., Irwin, K.E., Cruz, A.L.F., Wang, V., Rodríguez, J.L., Wong, P.C., and Ling, J.P. (2024). Large-scale RNA-seq mining reveals ciclopirox triggers TDP-43 cryptic exons. Preprint at bioRxiv. https://doi.org/10.1101/2024.03.27.587011.

- 77. Brown, A.L., Wilkins, O.G., Keuss, M.J., Hill, S.E., Zanovello, M., Lee, W.C., Bampton, A., Lee, F.C.Y., Masino, L., Qi, Y.A., et al. (2022). TDP-43 loss and ALS-risk SNPs drive mis-splicing and depletion of UNC13A. Nature 603, 131–137. https://doi.org/10.1038/s41586-022-04436-3.
- Ma, X.R., Prudencio, M., Koike, Y., Vatsavayai, S.C., Kim, G., Harbinski, F., Briner, A., Rodriguez, C.M., Guo, C., Akiyama, T., et al. (2022). TDP-43 represses cryptic exon inclusion in the FTD-ALS gene UNC13A. Nature 603, 124–130. https://doi.org/10.1038/s41586-022-04424-7.
- Prudencio, M., Humphrey, J., Pickles, S., Brown, A.L., Hill, S.E., Kachergus, J.M., Shi, J., Heckman, M.G., Spiegel, M.R., Cook, C., et al. (2020). Truncated stathmin-2 is a marker of TDP-43 pathology in frontotemporal dementia. J. Clin. Invest. 130, 6080–6092. https://doi.org/10.1172/10.130741
- Seddighi, S., Qi, Y.A., Brown, A.L., Wilkins, O.G., Bereda, C., Belair, C., Zhang, Y.J., Prudencio, M., Keuss, M.J., Khandeshi, A., et al. (2024). Mis-spliced transcripts generate de novo proteins in TDP-43-related ALS/FTD. Sci. Transl. Med. 16, eadg7162. https://doi.org/10.1126/sci-translmed.adg7162.
- Bellouze, S., Baillat, G., Buttigieg, D., de la Grange, P., Rabouille, C., and Haase, G. (2016). Stathmin 1/2-triggered microtubule loss mediates Golgi fragmentation in mutant SOD1 motor neurons. Mol. Neurodegener. 11, 43. https://doi.org/10.1186/s13024-016-0111-6.
- Krus, K.L., Strickland, A., Yamada, Y., Devault, L., Schmidt, R.E., Bloom, A.J., Milbrandt, J., and DiAntonio, A. (2022). Loss of Stathmin-2, a hallmark of TDP-43-associated ALS, causes motor neuropathy. Cell Rep. 39, 111001.
- Hodgson, R.E., Rayment, J., Huang, W.-P., Sanchez Avila, A., and Shelkovnikova, T.A. (2024). Opto-controlled C9orf72 poly-PR forms anisotropic condensates causative of TDP-43 pathology in the nucleus.. Preprint at bioRxiv. https://doi.org/10.1101/2024.03.05.581933.
- 84. Spence, H., Waldron, F.M., Saleeb, R.S., Brown, A.L., Rifai, O.M., Gilodi, M., Read, F., Roberts, K., Milne, G., Wilkinson, D., et al. (2024). RNA aptamer reveals nuclear TDP-43 pathology is an early aggregation event that coincides with STMN-2 cryptic splicing and precedes clinical manifestation in ALS. Acta Neuropathol. 147, 50. https://doi.org/10.1007/s00401-024-02705-1.
- An, H., Elvers, K.T., Gillespie, J.A., Jones, K., Atack, J.R., Grubisha, O., and Shelkovnikova, T.A. (2022). A toolkit for the identification of NEAT1\_2/paraspeckle modulators. Nucleic Acids Res. 50, e119. https://doi.org/10.1093/nar/gkac771.
- Kukharsky, M.S., Quintiero, A., Matsumoto, T., Matsukawa, K., An, H., Hashimoto, T., Iwatsubo, T., Buchman, V.L., and Shelkovnikova, T.A. (2015).
   Calcium-responsive transactivator (CREST) protein shares a set of structural and functional traits with other proteins associated with amyotrophic lateral sclerosis. Mol. Neurodegener. 10, 20. https://doi.org/10.1186/s13024-015-0014-y.
- 87. Budini, M., Romano, V., Quadri, Z., Buratti, E., and Baralle, F.E. (2015). TDP-43 loss of cellular function through aggregation requires additional structural determinants beyond its C-terminal Q/N prion-like domain. Hum. Mol. Genet. 24, 9–20. https://doi.org/10.1093/hmg/ddu415.
- Suzuki, K., Bose, P., Leong-Quong, R.Y., Fujita, D.J., and Riabowol, K. (2010). REAP: A two minute cell fractionation method. BMC Res. Notes 3, 294. https://doi.org/10.1186/1756-0500-3-294.
- Hulsen, T., de Vlieg, J., and Alkema, W. (2008). BioVenn a web application for the comparison and visualization of biological lists using area-proportional Venn diagrams. BMC Genom. 9, 488. https://doi.org/10.1186/1471-2164-9-488.
- Xie, Z., Bailey, A., Kuleshov, M.V., Clarke, D.J.B., Evangelista, J.E., Jenkins, S.L., Lachmann, A., Wojciechowicz, M.L., Kropiwnicki, E., Jagodnik, K.M., et al. (2021). Gene Set Knowledge Discovery with Enrichr. Curr. Protoc. 1, e90. https://doi.org/10.1002/cpz1.90.





#### **STAR**\***METHODS**

#### **KEY RESOURCES TABLE**

REAGENT or RESOURCE	SOURCE	IDENTIFIER
Antibodies		
Mouse Monoclonal anti-TDP-43	R&D Biosystems	Cat# MAB77781
Rabbit Polyclonal anti-TDP-43 C-terminal	Sigma	Cat# T1580
Rabbit Monoclonal anti-TDP-43 (E2G6G)	Cell Signaling	Cat# 89718
Rabbit Polyclonal anti-Flag tag (DYKDDDDK)	Proteintech	Cat# 20543-1-AP
Rabbit Polyclonal anti-pinin/PNN	Proteintech	Cat# 18266-1-AP
Mouse Monoclonal anti-coilin/p80	BD Biosciences	Cat# 612074
Rabbit Polyclonal anti-PML	Proteintech	Cat# 21041-1-AP
Rabbit Polyclonal anti-SAFB	Proteintech	Cat# 21857-1-AP
Rabbit Polyclonal anti-GFP	Proteintech	Cat# 50430-2-AP
Rabbit Polyclonal anti-STMN2	Proteintech	Cat# 10586-1-AP
Mouse Monoclonal anti-STMN2	Biotechne	Cat# MAB6930
Mouse Monoclonal anti-GFP	Proteintech	Cat# 66002-1-lg
Rabbit Polyclonal anti-NONO	Proteintech	Cat# 11058-1-AP
Rabbit Polyclonal anti-YBX1	Proteintech	Cat# 20339-1-AP
Rabbit Polyclonal anti-hnRNPC	Proteintech	Cat# 11760-1-AP
Mouse Monoclonal anti-NPM1	Proteintech	Cat# 60096-1-Ig
Rabbit Polyclonal anti-A11 oligomer	ThermoFisher	Cat# AHB0052
Rabbit Polyclonal anti-GAPDH	Proteintech	Cat# 10494-1-A
Biotinylated goat anti-rabbit IgG	Vector labs	Cat# BA-1000
Mouse IgG HRP Linked Whole Ab	Amersham	Cat# NA931
Rabbit IgG HRP Linked Whole Ab	Amersham	Cat# NA934
Secondary fluorescently-labeled antibodies: Alexa 488/546 Fluor anti-mouse/rabbit IgG	ThermoFisher	Cat# A-11008; A-11001; A-11030; A-11035
Bacterial and virus strains		
NEB® Stable Competent E. coli (High Efficiency)	New England Biolabs	Cat# C3040H
NEB® 5-alpha Competent E. coli (High Efficiency)	New England Biolabs	Cat# C2987H
Biological samples		
Human postmortem tissue (spinal cord)	London Neurodegenerative Diseases Brain Bank	request #1470
Chemicals, peptides, and recombinant proteins		
Actinomycin D	Sigma-Aldrich	Cat#A1410
Pladienolide B	Cayman Chemicals	Cat#16538
Urea	Sigma-Aldrich	Cat#U5128
SSC, 20× concentrate	Sigma-Aldrich	Cat#SRE0068
Formamide	Sigma-Aldrich	Cat#F9037
RNase A	New England Biolabs	Cat#T3018L
MG132	Sigma-Aldrich	Cat#M7449
Polyinosinic-polycytidylic acid	Sigma-Aldrich	Cat#P9582
NaAsO <sub>2</sub>	Sigma-Aldrich	Cat#S7400
1,6-hexanediol	Sigma-Aldrich	Cat#240117
Oligomycin A	Sigma-Aldrich	Cat#75351
2-deoxy-glucose	ApexBio	Cat#B1027
Polyinosinic-polycytidylic acid potassium salt, poly(l:C)	Sigma-Aldrich	Cat#P9582

(Continued on next page)



Continued		
REAGENT or RESOURCE	SOURCE	IDENTIFIER
Cycloheximide	Sigma-Aldrich	Cat#C7698
Poly-L-Lysine	Sigma-Aldrich	Cat#25988-63-0
Aqueous Glutaraldehyde EM Grade	EMS Diasum	Cat#16110
Bovine Serum Albumin (BSA)	Jackson ImmunoResearch	Cat#001-000-161
Disuccinimidyl glutarate (DSG)	Sigma-Aldrich	Cat#80424
Recombinant TDP-43	R&D Biosystems	Cat#AP-190-100
Critical commercial assays	· ·	
Herculase II Fusion DNA polymerase	Agilent	Cat#600675
Zero Blunt <sup>TM</sup> TOPO <sup>TM</sup> kit	ThermoFisher	Cat#450245
Lipofectamine2000 Transfection Reagent	ThermoFisher	Cat#11668027
M-MLV Reverse Transcriptase	Promega	Cat#M1701
qPCRBIO SyGreen Mix Lo-Rox	PCR Biosystems	Cat#PB20.11-05
GoTag® Green Master Mix	Promega	Cat#M712
JetPRIME Transfection Reagent	PolyPlus	Cat#101000027
GenElute <sup>TM</sup> Mammalian Total	Sigma-Aldrich	Cat#RTN350
RNA Miniprep Kit	Signia / lianon	Califfition
QIAzol Lysis Reagent	Qiagen	Cat#79306
Chromotek GFP-Trap® agarose	Proteintech	Cat#gta
STEMdiff <sup>TM</sup> Astrocyte Differentiation Kit	Stemcell Technologies	Cat#100-0013
RiboLock RNase inhibitor	ThermoFisher	Cat#EO0381
Vectastain ® ABC reagent Kit	Vector Labs	Cat#PK6100
ImPACT ® DAB reagent Kit	Vector Labs	Cat#SK-4103
RNase free DNase set	Qiagen	Cat#79254
Ni-NTA Superflow beads	Qiagen	Cat#30410
His-streptavidin	NKMAX	Cat#stv0801
cOmplete <sup>™</sup> , EDTA-free Protease	Roche	Cat#4693132001
Inhibitor Cocktail		
10% Mini-PROTEAN® TGX <sup>TM</sup> Precast Gel, 15-well	Bio-Rad	Cat#4561036
Clarity Max Western ECL Substrate	Bio-Rad	Cat#1705062
GelCode <sup>™</sup> Blue Safe Protein Stain	ThermoFisher	Cat#24594
Epredia <sup>TM</sup> Immu-Mount <sup>TM</sup>	ThermoFisher	Cat#10622689
Deposited data		
Raw and processed proteomics data for: 1) TC proteome; 2) soluble nuclear TDP-43 interactome	jPOST partner repository (https://jpostdb.org)	JPST003167 (PXD052963)
Experimental models: Cell lines		
Human: HeLa cells (ATCC)	Sigma-Aldrich	Cat#93021013
Human: SH-SY5Y neuroblastoma cells (ATCC)	Sigma-Aldrich	Cat#94030304
Human: neural precursors (Day 16),	Shelkovnikova	N/A
motor neurons (Day 42) and astrocytes derived from ES H9 line	et al. <sup>23</sup> and this paper	
Oligonucleotides		
Silencer Select®: TARDBP (s23829)	ThermoFisher	Cat#4392420
AllStars Negative Control siRNA	Qiagen	Cat#SI03650318
Oligo(dT)30-Cy5 DNA FISH probe	Sigma	N/A
Random hexamers	ThermoFisher	Cat#48190011
Primers for RT-qPCR and PCR, see Table S2	An et al. <sup>85</sup> ; Cao et al. <sup>50</sup> ; this paper	N/A

(Continued on next page)



Continued		
REAGENT or RESOURCE	SOURCE	IDENTIFIER
UG <sub>(x15)</sub> RNA oligonucleotide: [CY5] (UGUGUGUGUGUGUGUGUGUGUGUGUGUGUGUGUGUGUG	This paper	N/A
CA <sub>(x12)</sub> RNA oligonucleotide: [CY5] (CACACACACACACACACACACACA) [BIOTEG]	This paper	N/A
Recombinant DNA		
Plasmid: TDP-43 WT GFP-tagged on N terminus (pEGFP-C1)	Kukharsky et al. <sup>86</sup>	N/A
Plasmid: TDP-43 D169G GFP-tagged on N terminus (pEGFP-C1)	This paper	N/A
Plasmid: TDP-43 M337V GFP-tagged on N terminus (pEGFP-C1)	This paper	N/A
Plasmid: TDP-43 Y374X GFP-tagged on N terminus (pEGFP-C1)	This paper	N/A
Plasmid: TDP-43 E14A/E17A (2M) GFP-tagged on N terminus (pEGFP-C1)	This paper	N/A
Plasmid: TDP-43 ΔNTD GFP-tagged on N terminus (pEGFP-C1)	This paper	N/A
Plasmid: TDP-43 F147/149L GFP-tagged on N terminus (pEGFP-C1)	This paper	N/A
Plasmid: pFlag-TDP-43 WT	Budini et al. <sup>87</sup>	N/A
Plasmid: pFlag-TDP-43 F147/149L	Budini et al. <sup>87</sup>	N/A
Software and algorithms		
Harmony 4.9 High-Content Imaging and Analysis Software	PerkinElmer	https://www.revvity.com/gb-en/category/cellular-imaging-software
Adobe Photoshop CS3	Adobe	https://adobe-photoshop-cs3- update.en.softonic.com/
ZEN blue software	ZEISS	https://www.zeiss.com/microscopy/ en/products/software/zeiss-zen.html
R studio Version 2023.09.1 + 494	R core team (2023)	https://www.r-project.org/
GraphPad Prism 9	GraphPad Software, Inc	https://www.graphpad.com/ updates/prism-900-release-notes
CellSens Dimension software	Olympus	https://www.olympus-lifescience.com/ en/software/cellsens/
Other		
Olympus BX57 upright microscope equipped with ORCA-Flash 4.0 camera (Hamamatsu)	Olympus (Evident)	Custom
ZEISS LSM 800 confocal microscope with Airyscan 2	Zeiss	https://www.zeiss.com/microscopy/ en/products/light-microscopes/ confocal-microscopes.html
PerkinElmer Opera Phenix - HCS	PerkinElmer	https://www.revvity.com/gb-en/product/ opera-phenix-plus-system-hh14001000
CFX96 Touch Real-Time PCR Detection System	Bio-Rad	https://www.bio-rad.com/ru-ru/ product/cfx96-touch-real-time- pcr-detection-system?ID=LJB1YU15
Hamamatsu NanoZoomer XR slide scanner	Hamamatsu	https://nanozoomer.hamamatsu.com/jp/en.html
MatTek 35-mm glass bottom dish	MatTek	Cat#P35G-1.5-14-C
μCLEAR 384 well plate	Greiner	Cat#781092
PhenoPlate-96, black, optically clear bottom	PerkinElmer	Cat# 6055302

#### **Article**



#### **RESOURCE AVAILABILITY**

#### **Lead contact**

Requests for reagents and further information should be directed to the lead contact, Tatyana A. Shelkovnikova (t.shelkovnikova@sheffield.ac.uk).

#### **Materials availability**

All study materials are available from the corresponding author; a signed Material Transfer Agreement (MTA) may be required for transfer.

#### Data and code availability

- Data reported in the paper will be shared by the lead contact upon request. The mass spectrometry data have been deposited
  with the ProteomeXchange Consortium via the jPOST partner repository (https://jpostdb.org) and are publicly available as of
  the date of publication. The dataset identifier is listed in the key resources table.
- This paper does not report original code.
- Any additional information required to reanalyze the data reported in this work paper is available from the lead contact upon request.

#### **EXPERIMENTAL MODEL AND STUDY PARTICIPANT DETAILS**

#### **Cell lines**

HeLa and SH-SY5Y cell lines (both ATCC) were obtained via Sigma. NPCs and motor neurons were differentiated from hES H9 cells and cultured as described in detail previously. Astrocytes were derived from hES cells using STEMdiff Astrocyte Differentiation Kit (StemCell technologies) according to the manufacturer's instructions.

#### **Human tissue**

Human postmortem tissue (spinal cord) was provided by the London Neurodegenerative Diseases Brain Bank (request #1470). Consent was obtained from all subjects for autopsy, histopathological assessment and research in accordance with local and national Ethics Committee approved donation. Information on the sex and age of donors was not provided by the Bank as part of this tissue request.

#### **METHOD DETAILS**

#### **Plasmids**

Plasmid for the expression of TDP-43 with GFP tag on its N terminus in pEGFP-C1 vector (Clontech) was generated in our previous study. <sup>86</sup> Mutations were introduced by standard cloning/PCR mutagenesis approaches. TDP-43 F147/149L and WT FLAG tag plasmids <sup>87</sup> were a gift from E. Buratti.

#### **Cell transfection and treatment**

Cell transfection with siRNA or plasmids was performed using either Lipofectamine2000 (ThermoFisher) or jetPRIME (PolyPlus). For high-content imaging, cells were plated on PhenoPlate-96 (black, optically clear bottom, PerkinElmer). Cells were treated with 500  $\mu$ M NaAsO<sub>2</sub> (250  $\mu$ M for hMNs), 10  $\mu$ M MG132, 5  $\mu$ g/mL of actinomycin D, 5  $\mu$ M oligomycin A, 10  $\mu$ g/mL cycloheximide (all Sigma), 25 mM 2-deoxy-glucose (ApexBio) and 50 nM pladienolide B (Cayman chemicals), as indicated in the figure legend/text. Cells were transfected with 250 ng poly(I:C) (Sigma) per well (24-well plate). For recovery, NaAsO<sub>2</sub>-containing media was replaced with fresh media after 1 h. Heat stress was induced by placing cells at 42°C for 45 min.

#### **Immunofluorescence**

Immunostaining with commercial antibodies (see key resources table, all at 1:1000 dilution) and RNA-FISH using a Cy5-labeled poly- $dT_{(x30)}$  DNA oligonucleotide probe (Sigma) were performed as described earlier. For formamide extraction of soluble protein, PFA-fixed cells permeabilized with methanol cells were incubated in 50% formamide/2xSSC buffer ON at 37°C, washed with 1xPBS and immunostained.

#### **Cell microscopy and quantification**

Images were taken using Olympus BX57 upright microscope equipped with ORCA-Flash 4.0 camera (Hamamatsu) and cellSens Dimension software (Olympus). Time-lapse microscopy was done on Opera Phenix HCS or Operetta CLS followed by analysis on Harmony 4.9 software (all PerkinElmer). Super-resolution imaging was done on ZEISS LSM 800 confocal microscope with Airyscan 2. Condensate quantification was performed either using custom automated pipelines on Harmony 4.9, or using ImageJ (Analyze particles tool), or manually in a blinded manner (indicated in figure legend in each case). Fluorescence intensity in the





nucleus/cytoplasm of cells was measured in Harmony 4.9 using the in-built intensity measurement tool or in a defined ROI using the respective ImageJ tool. Profiles were drawn using ImageJ.

#### **FRAP** analysis

Cells were grown and transfected on glass-bottomed 35-mm dishes (Mattek). 24 h post-transfection cells were treated and imaging was done in a  $CO_2$ /temperature control equipped chamber of a ZEISS LSM 800 confocal microscope, with a 63× oil immersion objective. Typically, three condensates were analyzed per cell for at least 10 cells per condition in a single experiment. A circular ROI ( $\sim$ 0.15  $\mu$ m in diameter) within the condensate or full condensate was bleached using a 488 nm laser. Images were acquired pre-bleaching, immediately after bleaching and then at  $\sim$ 200 ms intervals during recovery. The mean fluorescence intensity within the ROI was determined for each image using ZEN blue software (Zeiss). Intensity values were corrected for loss of fluorescence during imaging and normalized to pre-bleach fluorescence intensity. Average values were plotted and FRAP curves were fitted using a one-phase association equation in GraphPad Prism 9 software.

#### **RNA** expression analysis

For gene expression analysis studies, total RNA was extracted from cells grown in a 12-well format using Genelute total mammalian RNA kit (Sigma) or Qiazol (Qiagen). First-strand cDNA synthesis was performed using 500 ng of RNA with random primers (ThermoFisher) and MMLV reverse transcriptase (Promega) as per manufacturer's protocol. PCR was performed using GoTaq Green Master Mix (Promega). RT-qPCR was performed using qPCRBIO SyGreen Lo-ROX (PCRbio), and GAPDH was used for normalization. Primer sequences are given in Table S2.

#### TDP-43 solubility analysis and western blotting

Total cell lysates were prepared for western blot by adding  $2 \times SDS$ -PAGE loading buffer directly to the wells in a 24-well plate followed by denaturation at  $100^{\circ}C$  for 10 min. SDS-PAGE and detection of proteins were carried out as described elsewhere, <sup>85</sup> except Licor imager was used for detection. Briefly, samples were run on 10% Mini-PROTEAN TGX precast gels and transferred to PVDF membrane (Hybond P, Amersham) by semi-dry transfer. All washes were done in TBST. Blocking and antibody incubation were performed in 4% non-fat milk/TBST. Signal was visualized by Clarity Max Western ECL Substrate (Bio-Rad). For TDP-43 solubility analysis, cells were lysed in 1% Triton X-100/PBS buffer for 30 min at RT with periodic vortexing and then centrifuged at 17,000g for 20 min to obtain supernatant and pellet.  $2\times$  loading buffer was added to the supernatant and pellet, and pellet was vortexed prior to heating, to ensure full solubilization. For TDP-43 dimer detection, snap-frozen cell pellets were resuspended in  $1\times$ PBS with cOmplete mini proteasome inhibitor cocktail (Roche) supplemented with  $400~\mu$ M disuccinimidyl glutarate (DSG) (Sigma) and incubated for 30 min at RT with rotation. After quenching with 20 mM Tris base (pH 7.4) for 15 min, samples were mixed with an equal volume of  $2\times$  SDS-PAGE loading buffer. Commercial antibodies used are given in key resources table. Uncropped western blots are provided in Figure S9.

#### TDP-43 condensate isolation and stability analysis

HeLa cells were transfected to express TDP-43 GFP for 24 h, treated for 1 h with NaAsO $_2$  and left to recover for 2 h. Protocol for TC isolation was adapted from the paraspeckle purification protocol. <sup>41</sup> Cells were scraped in SG lysis buffer (50 mM Tris HCl, pH 7.4, 100 mM KOAc, 2 mM MgOAc, 0.5 mM DTT, 50  $\mu$ g/mL heparin, and 0.5% NP-40, cOmplete Mini - EDTA-free, RiboLock). Cells were lysed by passing through a 25G needle seven times on ice and nuclei were pelleted at 1000 g for 5 min at 4°C. Nuclei were washed, resuspended in the lysis buffer supplemented with 400 mM NaCl and left to lyse on ice for 30 min with periodic vortexing; efficiency of nuclear lysis was monitored under fluorescent microscope. Nuclear lysates were centrifuged at 1000 g for 5 min at 4°C to remove debris, and the supernatant containing TCs was centrifuged at 17000 g for 15 min at 4°C to obtain TC-enriched fraction. TC preparations were subjected 2M urea, 2% SDS, 2.5% 1,6-hexanediol, 1% Triton X-100 (all Sigma) or 10  $\mu$ g/mL RNase A (New England Biolabs) for 30 min in 1xPBS, and TC integrity was analyzed under the microscope (droplet covered with a coverslip; ×20 magnification) with subsequent quantification using 'Analyze particles' function of ImageJ.

#### **TDP-43** condensate proteomic analysis

TDP-43 condensates were isolated as described above from stressed HeLa cells and affinity purified using GFP-Trap agarose (Chromotek), by incubating beads for 3 h with TC suspension in SG lysis buffer. After several washes in the lysis buffer, the beads were snap-frozen in a minimal buffer volume. The samples were run on a 10% SDS-PAGE gel and each gel lane was excised for in-gel tryptic digestion using a DigestPro automated digestion unit (Intavis Ltd.). The resulting peptides in 1% (v/v) formic acid were fractionated using an Ultimate 3000 nano-LC system (Acclaim PepMap C18 LC column, Thermo Scientific) in line with an Orbitrap Fusion Tribrid mass spectrometer (Thermo Scientific). A 150 min gradient segments were performed using solvent A containing 0.1% formic acid and solvent B containing 80% acetonitrile in 0.1% formic acid with a flow rate of 300 nL/min. Peptides were ionized by nanoelectrospray ionization at 2.2 kV using a stainless-steel emitter with an internal diameter of 30 μm (Thermo Scientific) and a capillary temperature of 275° C. All spectra were acquired by Xcalibur 2.1 software (Thermo Scientific) and operated in data-dependent acquisition mode. FTMS1 spectra were collected at a resolution of 120,000 over a scan range (m/z) of 350–1550, with an automatic gain control (AGC) target of 400,000 and a max injection time of 100ms. Precursors were filtered according to charge state (to include



charge states 2–7), with monoisotopic peak determination set to peptide and using an intensity range from 5E3 to 1E20. Previously interrogated precursors were excluded using a dynamic window (40s +/-10ppm). The MS2 precursors were isolated with a quadrupole mass filter set to a width of 1.6m/z. ITMS2 spectra were collected with an AGC target of 5000, max injection time of 50ms and HCD collision energy of 35%. The raw data files were processed and quantified using Proteome Discoverer software v2.1 (Thermo Scientific) and searched against the UniProt Human database (downloaded January 2023; 81579 sequences) using the SEQUEST HT algorithm. Peptide precursor mass tolerance was set at 10ppm, and MS/MS tolerance was set at 0.6Da. Search criteria included oxidation of methionine (+15.995Da), acetylation of the protein N terminus (+42.011Da) and Methionine loss plus acetylation of the protein N terminus (-89.03Da) as variable modifications and carbamidomethylation of cysteine (+57.021Da) as a fixed modification. Searches were performed with full tryptic digestion and a maximum of 2 missed cleavages were allowed. The reverse database search option was enabled and all data was filtered to satisfy false discovery rate (FDR) of 5%. GFP-only samples were used as a background control. Pulldown experiment was performed twice in duplicates, and the results from two independent experiments were combined. Mass spectrometry analysis and data processing was done as described above.

#### **Soluble TDP-43 interactome analysis**

To obtain the TDP-43 GFP interactome in unstressed cells, the nuclear fraction was isolated from HeLa cells expressing TDP-43 GFP, according to a previously published "REAP" protocol. Briefly, cells grown on 6-cm dishes were scraped in 500  $\mu$ L of ice-cold 1xPBS and centrifuged at 2000 rpm for 2 min. Pelleted cells were resuspended in 200  $\mu$ L of ice-cold 0.1% NP40/PBS and triturated 5 times with a P1000 pipette tip. Nuclei were pelleted at,000 rpm for 2 min, lysed in 1% Triton X-100/PBS using needle shearing and vortexing and subjected to GFP-Trap pulldown. GFP-only samples were used as a background control. Pulldown experiment was performed twice in duplicates, and the results from two independent experiments were combined. Mass spectrometry analysis and data processing was done as described above.

#### **Confocal nanoscanning (CONA)**

Prior to the assay, transfected cells in a 35-mm dish were lysed in 500  $\mu$ L of 1% Triton X-100/PBS and 40U/mL RiboLock for 15 min on ice with periodic vortexing, and lysates were cleared by centrifuging at 13000 rpm for 15 min, snap-frozen and kept in  $-80^{\circ}$ C. RNA oligonucleotides (5′ end labeled with Cy5 and 3′ labeled with biotin-TEG) were custom-made and HPLC-purified by Eurofins. Ni-NTA Superflow beads (Qiagen, 30410) were washed with binding buffer (0.3 M NaCl, 20 mM HEPES pH 7.5, 0.01% Triton X-100, 5 mM MgCl<sub>2</sub>) and resuspended to 50% slurry. 40 pmol of His-streptavidin (NKMAX) was mixed with 25  $\mu$ L of beads (50% slurry) for 30 min with shaking/rotating at RT. Beads were washed in binding buffer 3 times and resuspended in binding buffer. RNA oligonucleotide (50 pmol) was added to 25  $\mu$ L of the streptavidin beads and incubated for 30 min with shaking/rotating at RT. Beads were washed in binding buffer with MgCl<sub>2</sub> 3 times and resuspended in 25  $\mu$ L of the same buffer. 5  $\mu$ L beads was added to thawed cell lysates (100  $\mu$ L) containing an equal amount of GFP-tagged proteins (normalized by western blot) and incubated with shaking/rotating at RT for 2 h. Lysates were used within 15 min of thawing. Beads were washed in binding buffer three times and 30  $\mu$ L beads was transferred to  $\mu$ CLEAR 384 well plate (Greiner, 781092). Imaging was done on Opera Phenix with the following parameters: brightfield: 20 ms, 50%, 2.0  $\mu$ m; Cy5: 100 ms, 50%, 2.0  $\mu$ m; number of planes 3; distance 0.5  $\mu$ m; last plane at 17.0  $\mu$ m; overall height 1  $\mu$ m. Beads both in the center and on the periphery of the well were included in the analysis. Mean ring intensity for Cy5 and EGFP channels were quantified using a custom pipeline for ring segmentation on Harmony 4.9 (details available upon request).

#### In vitro analysis of recombinant TDP-43 assemblies

Recombinant TDP-43 (R&D Biosystems, AP-190-100) (kept in  $-80^{\circ}$ C) was thawed on ice and resuspended in the assay buffer (20 mM Tris-HCl pH7.5, 20 mM KCl, 2 mM MgCl<sub>2</sub> and 1mM DTT) at a final concentration of 1.25  $\mu$ M. Sample was depleted of large preformed assemblies where indicated by centrifuging at 1000 g for 5 min. Samples were incubated for the indicated amount of time at RT in a low-binding microcentrifuge tube with or without RNA oligonucleotide (equimolar concentration) or HeLa total RNA (25 ng/ $\mu$ L). Samples were then placed on a coverslip in a 5- $\mu$ L microdroplet and left for 15 min. TDP-43 assemblies sedimented on the coverslip were fixed with 4% glutaraldehyde (1:1 ratio) for 30 min. Coverslips were washed with 1xPBS twice, blocked with 1xPBS containing 1% BSA for 1 h at RT and incubated with anti-TDP-43 antibody (rabbit polyclonal, Sigma-Aldrich, T1580, 1:5000) diluted in blocking buffer for 2 h at RT. Secondary Alexa 488 Fluor antibody (ThermoFiher) was used for detection (1:1000, 1 h at RT). Coverslips were mounted on a glass slide using Immu-Mount (ThermoFisher). Images were taken using Olympus BX57 upright microscope and ORCA-Flash 4.0 camera and processed using cellSens Dimension software (Olympus). Quantification of assemblies was done using 'Analyze particles' tool of ImageJ.

#### **Immunohistochemistry**

Deparaffinized and rehydrated tissue sections (7-μm thick) were incubated in 3% hydrogen peroxide in methanol for 20 min and subjected to antigen retrieval in 10 mM sodium citrate (pH 6.0) in a pressure cooker. Blocking and all washes were done using TBST as the base buffer. Sections were incubated in 10% goat serum/TBST for 1 h and then in the primary antibody (TDP-43 E2G6G, 1:500) diluted in blocking solution at 4°C overnight. After several washes in TBST, slides were incubated with biotinylated goat anti-rabbit IgG (VectorLab) in TBST (1:1000) for 1 h at RT. Vectastain Elite ABC HRP kit and ImPACT DAB kit (both VectorLabs) were used for





detection according to manufacturer's instructions. Slides were then washed in distilled water, sections were dehydrated, cleared in xylene and coverslips mounted using DPX resin. Hamamatsu NanoZoomer XR slide scanner was used for imaging.

#### **QUANTIFICATION AND STATISTICAL ANALYSIS**

#### Mass spectrometry data processing

Datasets were processed using R packages readr, dplyr, and ggplot2 packages. After removing common contaminants, the dataset replicates (technical and biological) were merged for each condition. A cut-off of  $\geq 2$  total peptide count was utilized, and only the proteins enriched relative the GFP-only "background" dataset were taken into further analysis. Peptide IDs were then converted into gene names using Uniprot (https://www.uniprot.org/id-mapping). Dataset overlaps were visualized using BioVenn online tool. <sup>89</sup> Enrichment analysis was done using Enrichr online tool, <sup>90</sup> and visualization was done in Excel.

#### Statistical analysis

Statistical analysis was performed using GraphPad Prism 9 software. N indicates the number of biological replicates. All statistical tests are indicated in the figure legends. Graphs represent mean ± SEM unless stated otherwise.